UC Santa Barbara
UC Santa Barbara Previously Published Works

Title

Three-Dimensional Acoustic Multipole Waveform Inversion at Yasur Volcano, Vanuatu

Permalink

https://escholarship.org/uc/item/4r13b4wr

Journal

Journal of Geophysical Research: Solid Earth, 124(8)

ISSN

2169-9313

Authors

Iezzi, AM
Fee, D
Kim, K
et al.

Publication Date

2019-08-01

DOI

10.1029/2018jb017073

Copyright Information

Peer reviewed

Three-Dimensional Acoustic Multipole Waveform Inversion at Yasur Volcano, Vanuatu

A. M. Iezzi[1] (ID), **D. Fee[1]** (ID), **K. Kim[2]** (ID), **A. D. Jolly[3]** (ID), **and R. S. Matoza[4]** (ID)

[1]Geophysical Institute, Alaska Volcano Observatory, University of Alaska Fairbanks, Fairbanks, AK, USA, [2]Lawrence Livermore National Laboratory, Livermore, CA, USA, [3]GNS Science, Lower Hutt, New Zealand, [4]Department of Earth Science and Earth Research Institute, University of California, Santa Barbara, CA, USA

Abstract Acoustic waveform inversions can provide estimates of volume flow rate and erupted mass, enhancing the ability to estimate volcanic emissions. Previous studies have generally assumed a simple acoustic source (monopole); however, more complex and accurate source reconstructions are possible with a combination of equivalent sources (multipole). We deployed a high-density acoustic network around Yasur volcano, Vanuatu, including acoustic sensors on a tethered aerostat that was moved every ∼15–60 min. Using this unique data set we invert for the acoustic multipole source mechanism using a grid search approach for 80 events to examine volume flow rates and dipole strengths. Our method utilizes finite-difference time-domain modeling to obtain the full 3-D Green's functions that account for topography. Inversion results are compared using a monopole-only, multipole (monopole and dipole), simulations that do not include topography, and those that use a subset of sensors. We find that the monopole source is a good approximation when topography is considered. However, initial compression amplitude is not fully captured by a monopole source so source directionality cannot be ruled out. The monopole solution is stable regardless of whether a monopole-only or multipole inversion is performed. Inversions for the dipole components produce estimates consistent with observed source directionality, though these inversions are somewhat unstable given station configurations of typical deployments. Our results suggest that infrasound waveform inversion shows promise for realistic quantitative source estimates, but additional work is necessary to fully explore inversion stability, uncertainty, and robustness.

1. Introduction

Volcanic eruptions emit a considerable amount of acoustic energy in the infrasonic band (acoustic signals <20 Hz) with minimal absorption that can be recorded from local (<15 km) to global (>250 km) distances and used to detect, locate, and quantify volcanic emissions in real time (e.g., Fee & Matoza, 2013; Matoza et al., 2019). Acoustic waveform inversions can provide estimates of volume flow rate and mass eruption rate, which are invaluable parameters for volcano monitoring and ash transport models (Fee et al., 2017; Kim et al., 2015). Similar methods can be applied to anthropogenic sources to estimate explosion yield (Kim & Rodgers, 2016).

Acoustic signals from volcanic explosions comprise the source as well as propagation effects the wave encounters along the path from the source to receiver (e.g., topography, atmospheric conditions). Proper modeling of these propagation effects allows the unknown acoustic source parameters of the explosion to be recovered from the recorded waveforms (e.g., Kim et al., 2015). While some studies have shown that atmospheric conditions can be retrieved from acoustic waveforms (e.g., Johnson et al., 2012; Ortiz et al., 2018), they are often assumed to have negligible impact on the acoustic waveforms at local distances of less than a few kilometers (e.g., Fee et al., 2017; Johnson & Miller, 2014; Kim et al., 2015). However, numerous studies (e.g., Fee et al., 2017; Kim & Lees, 2014; Kim et al., 2015; Lacanna & Ripepe, 2013; Matoza et al., 2009) have established that the local topography of a volcanic edifice can affect the recorded waveforms and therefore the calculation of mass flow rate via waveform source inversion. Therefore, it is important to account for topography in acoustic source inversions for locations with intricate topographic features (i.e., most volcanoes).

Previous volcanic studies have generally assumed a simple volumetric acoustic source (monopole); how-ever more complex and accurate source reconstructions can be estimated using a combination of pressure

a)   b)
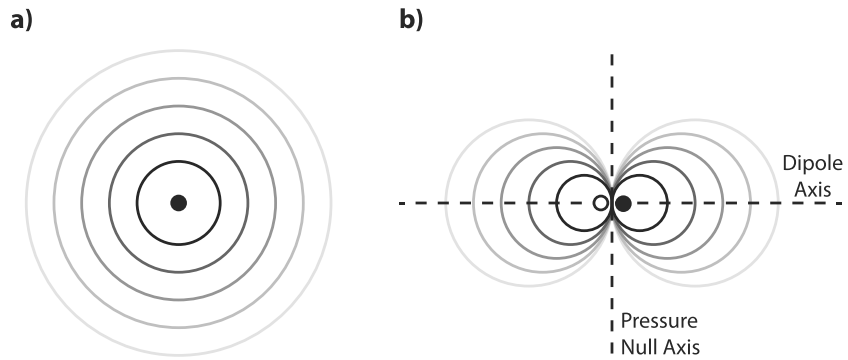
Figure 1. Radiation pattern of an acoustic (a) monopole and (b) dipole. Black and white circles represent positive and negative monopole sources, respectively.

fluctuations from volume changes and shifts in momentum of a fluid (multipole) (Johnson et al., 2008; Kim et al., 2012). The actual acoustic source is likely dependent on the type of volcanic activity, where blast-type explosions may be best represented by a simple volumetric source (Fee & Matoza, 2013; Fee et al., 2017; Johnson, 2003; Kim et al., 2015; Matoza et al., 2014; Woulff & McGetchin, 1976), while sustained eruptions likely have a more complicated mechanism similar to jet noise (Matoza et al., 2009, 2013).

Our study aims to determine if acoustic directionality is resolvable and explore the stability of both monopole and multipole source inversions of discrete explosions of Yasur volcano by sampling the wavefield in both the horizontal and vertical directions. Our deployment consists of a traditional deployment of infrasound sensors on the ground surface, as well as a sensor onboard a tethered aerostat that was fixed at various locations around the volcanic crater, capturing explosions from a variety of azimuths and inclinations (Jolly et al., 2017). We use finite-difference time-domain (FDTD) modeling to obtain the full 3-D Green's functions for each propagation path from source to receiver. This method, following Kim and Lees (2014), takes into account realistic topography based on a high-resolution digital elevation model created using structure-from-motion techniques. We then invert for the minimum error solution source location and acoustic source mechanism using a grid search approach (Kim et al., 2015). We perform this inversion for 80 events from the two vents of Yasur to examine the source characteristics of the vents, including an infrasound-derived volume flow rate as a function of time and acoustic radiation directionality after the influences of topography are removed.

2. Background

2.1. Acoustic Multipole Sources

A well-constrained acoustic source inversion requires extensive station coverage in order to fully sample the wavefield (Kim et al., 2012). If the acoustic source region is compact (small compared to the wavelength of interest), the source can be represented as a sum of equivalent point sources (Kim et al., 2012; Matoza et al., 2013). An acoustic multipole source mechanism is a combination of pressure fluctuations from monopole, dipole, and quadrupole sources (Lighthill, 1952). A monopole (or simple) source represents the net change of mass flow rate in a compact source region. Lighthill (1978) defines the pressure at time t and distance r resulting from a monopole source as

$$p(t, r) = \frac{\dot{S}(t - r/c)}{4\pi r} \tag{1}$$

where $\dot{S}$ is the source strength (rate of change of the mass flow rate) and c is the speed of sound. The monopole generates sound that radiates equally in all directions (Figure 1a). The dipole source is equivalent to force or momentum changes within the fluid (i.e., no net introduction of fluid) and can be represented by two closely spaced (with respect to the acoustic wavelength) monopoles that are out of phase by 180° (Figure 1b). The acoustic dipole results in directivity of the acoustic radiation pattern, where there is zero pressure change orthogonal to the dipole axis (pressure null axis) and the maximum pressure change exists at the dipole axis (Johnson et al., 2008; Lighthill, 1952). Dipole source mechanisms are less efficient than a monopole source since the two alternating simple sources have a combined radiation pattern that cancels much of the radiated energy (Kim et al., 2012; Lighthill, 1952). Dipole sources can be combined to

form higher-order source terms (lateral and longitudinal quadrupoles, etc.). In this study, we focus on the monopole and dipole components and refer to their combination as a multipole.

Volcanoes erupt in a variety of styles including lava fountaining and effusive activity (Hawaiian), discrete blasts (Strombolian and Vulcanian), and high-energy sustained ash emissions (Subplinian-Plinian). While impulsive, blast-type volcanic explosions such as those common to Yasur volcano have been shown to be well approximated by a monopole source (e.g., Fee & Matoza, 2013; Fee et al., 2017; Johnson, 2003; Kim et al., 2015; Witsil & Johnson, 2018; Woulff & McGetchin, 1976), higher-order acoustic terms might also be present and provide valuable information about the eruption (De Angelis et al., 2016; Johnson et al., 2008).

Multipole radiation can be expressed as a combination of a monopole, horizontal dipole, and vertical dipole (Johnson et al., 2008; Kim et al., 2012). The vertical dipole has previously been neglected for many studies of volcanic eruptions due to infrasound sensors only being placed on the Earth's surface (Matoza et al., 2013). Johnson et al. (2008) solved for a subvertical dipole orientation where sensors located on the crater rim were above the crater floor. Studies such as McKee et al. (2017) and Rowell et al. (2014) have taken advantage of surrounding topography for network deployments at Aso and Karymsky volcanoes, respectively, in order to improve vertical coverage of infrasound sensors; however, not all volcanoes have the advantage of nearby high relief topography. This study, for the first time, incorporates the vertical dipole component using acoustic data collected on a tethered aerostat, which has great flexibility for sensor location and may sample closer to a hypothetical vertical dipole axis.

2.2. Acoustic Source Inversion

Waveform inversion techniques allow the construction of quantitative source models for a wide range of volcanic processes and hence have become popular for the studies of both seismic (e.g., Chouet et al., 2005; Ohminato et al., 1998) and acoustic (e.g., Johnson et al., 2008; Kim et al., 2012, 2015) data. Previous infrasound studies have assumed monopole (e.g., Fee et al., 2017; Johnson & Miller, 2014; Kim & Lees, 2011; Kim et al., 2015), dipole (e.g., Caplan-Auerbach et al., 2010; Lamb et al., 2015), and multipole (e.g., De Angelis et al., 2016; Johnson et al., 2008; Kim et al., 2012) source mechanisms. Additionally, many studies have compared infrasound-derived gas volumes with UV camera data (e.g., Dalton et al., 2010; Delle Donne et al., 2016), visual camera (e.g., Johnson & Miller, 2014; Witsil & Johnson, 2018), thermal imagery (e.g., De Angelis et al., 2016), and ground-based (e.g., Fee et al., 2017) and satellite (e.g., Albert et al., 2015) ash and gas emission estimates. These multidisciplinary studies have allowed for greater insight into the acoustic source mechanism by using independent measures to compare with the infrasound results. However, these comparisons are complicated by the fact that all methods have their own inherent assumptions and associated errors.

A few studies have inverted for the combined monopole and dipole source mechanism, though none have incorporated the effects of topography and numerical Green's functions. Johnson et al. (2008) inverted for the volume flux of a volcanic explosion using the monopole-only, dipole-only, and multipole source mechanisms for lava lake explosions at Mt. Erebus, Antarctica. They found that the initial tearing of the bubble membrane likely radiated as a dipole source that transitions into a predominantly monopole source as the bubble membrane is fully compromised. Kim et al. (2012) performed multipole (monopole and dipole) source inversions for explosions at Tungurahua volcano, Ecuador and concluded that the observed strong directivity of infrasound radiation can be explained by an "effective dipole" largely resulting from volcanic crater topography preferentially directing the sound radiation.

At local distances, topography can alter the recorded acoustic waveforms. Therefore, constraining the effects of topography has proven important for acoustic source inversions (Kim & Lees, 2014; Kim et al., 2015). The FDTD code used in this study to constrain topographic influences was first published in Kim and Lees (2011), where diffraction of acoustic waves on the vent rim edge was observed both in recorded and synthetically produced waveforms at Karymsky volcano, Russia. Lacanna and Ripepe (2013) used a FDTD method in 2-D Cartesian coordinates to constrain the influence of topography on the acoustic wavefield assuming a simple monopole source. Kim and Lees (2014) incorporated a digital elevation model for the FDTD forward model to calculate the full 3-D Green's functions, finding that including effects of topography can improve reverse time modeling techniques for source localization. Kim et al. (2015) then used the updated FDTD forward model methods from Kim and Lees (2014) and source inversion work by Kim et al. (2012) to invert for the monopole source time function, finding that a monopole source was sufficient to accurately model explosions at Sakurajima volcano, Japan. Kim et al. (2012) and Lacanna and Ripepe (2013) showed
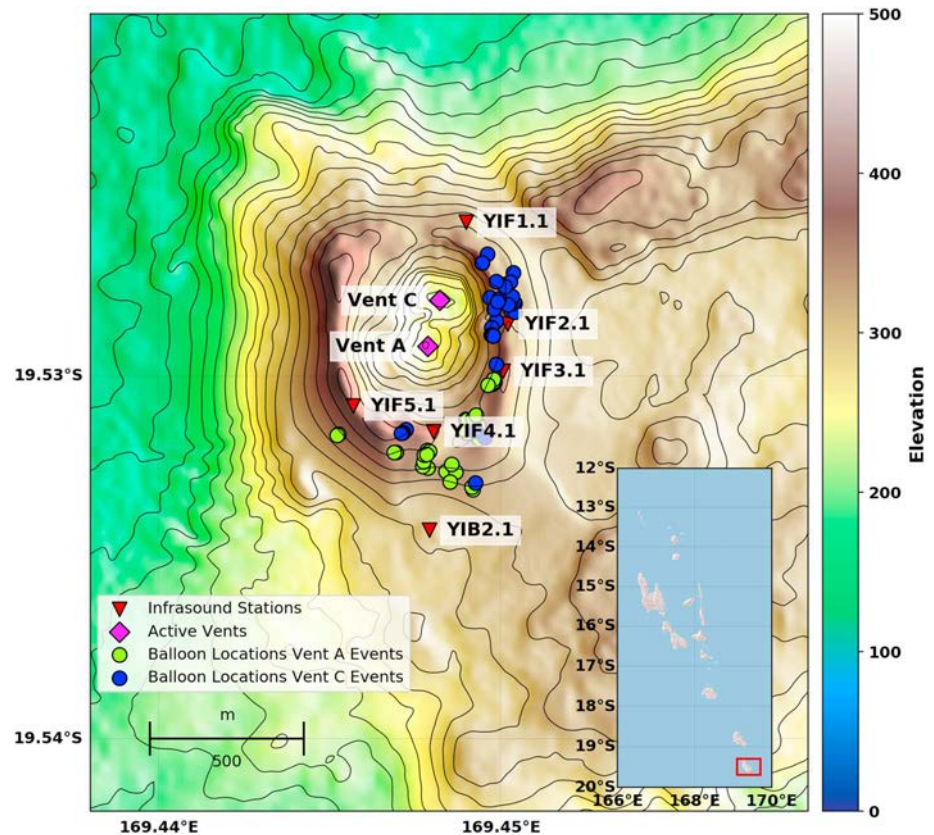
Figure 2. Yasur location map and sensor deployment. The volcanic edifice is represented by the digital elevation model using 20-m contour intervals. Red inverted triangles represent infrasound stations used in this study, pink diamonds represent active vents (Vent C is north and Vent A is south), and green and blue circles show the aerostat locations in the *x-y* plane for the Vent A and Vent C explosions used in this study, respectively. Inset shows the location of Yasur volcano in the Vanuatu archipelago.

that neglecting topography for acoustic waveform inversions can lead to large source estimation errors and should therefore be accounted for. More recently, the methods laid out in Kim et al. (2015) were extended to determine total erupted mass and then compared with independent estimates derived from ash collection systems and gas measurements by Fee et al. (2017), finding good agreement between the two methods.

While previous work has focused on quantifying the volume and mass flow rates for volcanic eruptions, a multipole acoustic waveform inversion that includes both the vertical dipole component and accounts for 3-D topography simultaneously has not been performed. Here we build upon these previous studies by using the inversion method of Kim et al. (2015) and including the multipole source. By accounting for topography to create the synthetic waveforms, we can examine how much of the observed directive radiation pattern (Jolly et al., 2017) is due to topography or source directivity (i.e., a dipole source mechanism), a problem evident in Kim et al. (2012) that has remained undetermined.

2.3. Yasur Volcano, Vanuatu

Yasur volcano (360 m above sea level) is a basaltic to basaltic-andesitic scoria cone located on the island of Tanna, Vanuatu. Activity is characterized by continuous gas emissions punctuated by frequent Strombolian to Vulcanian explosive activity for at least the past 300 years (Simkin et al., 1981). Eruption rates at Yasur are high, with up to several explosions per minute (Battaglia et al., 2016b; Meier et al., 2016). Passive degassing composition differs from that of gases released by explosions, suggesting explosions are driven by deep volatile exsolution (Métrich et al., 2011), which is typical for volcanoes with Strombolian activity. The 400-m-wide summit crater is divided into two subcraters, North (Vent C) and South (Vents A and B) (Figure 2). Yasur's multiple vents are thought to come from a single homogeneous magma supply based on seismic (Kremers et al., 2013) and petrologic (Kremers et al., 2012) evidence. Yasur is a prolific and reliable source of infrasound which is regularly detected as far as 600 km and used to validate and update wind

models (Assink et al., 2014; Le Pichon et al., 2005). A number of recent studies have focused on seismic and infrasound signals at Yasur volcano and their relation to other multidisciplinary data sets including UV, thermal imagery, and Doppler radar (e.g., Battaglia et al., 2016a, 2016b; Jolly et al., 2017; Kremers et al., 2013; Marchetti et al., 2013; Meier et al., 2016).

3. Methods

3.1. Data Collection

The field campaign at Yasur occurred in July to August 2016 and was a joint effort between the University of Alaska Fairbanks (UAF), University of California Santa Barbara (UCSB), GNS New Zealand, University of Canterbury in New Zealand, and the Vanuatu Meteorology and Geohazards Department. We focus on data from six ground-based Chaparral Physics Model 60 UHP infrasound sensors, five located around the crater rim (YIF1-5) and one ~1 km from the vent (YIB2.1) (Figure 2). An infraBSU-type sensor was deployed on the aerostat. This sensor uses a MEMS transducer with an operation similar to that described in Marcillo et al. (2012). Because the aerostat sensor was in a different location for every explosion, we name them as separate stations (and therefore events) as YBAL.3(vent; event number). Chaparral Physics Model 60 UHP infrasound sensors have a flat response between 33 s to Nyquist and pressure range of ±1,000 Pa, and were sampled at 400 Hz. The BSU-type sensor with flat response from 30 s to Nyquist on the aerostat were sampled at 200 Hz. Infrasound data were digitized using the Omnirecs DATA-CUBE digitizers.

The aerostat operated from 29 July to 1 August 2016 during the daytime hours and was moved every 15–60 min to a new stationary tether position. By the end of the experiment, the aerostat occupied 38 loiter positions that spanned ~200° in azimuth and 50° in takeoff angle (defined as the angle viewed from the eruption crater with vertical equal to 90°) (Jolly et al., 2017). The five crater stations spanned an azimuth of 207°. Unfortunately, a sixth crater station (YIF6.1) located to the northwest side only had data for 28 July to 29 July, leaving an azimuthal gap in acoustic wavefield coverage for nearly the entire experiment when the tethered aerostat sensor was deployed. Therefore, we do not use YIF6.1 in our study as we favor data collected aboard the tethered aerostat. In addition to the acoustic equipment, the campaign included eight broadband seismometers, an unmanned aerial vehicle (UAV) supplemented by survey-grade GPS, high-definition video, multiangle GoPro video, forward looking infrared camera (FLIR), and Fourier transform infrared spectroscopy (FTIR). However, we focus only on infrasound data in this study. Jolly et al. (2017) describe the details on the aerostat deployment and observations.

3.2. DEM Creation

At local distances, previous studies have indicated that topography can largely affect acoustic waveforms (e.g., Kim & Lees, 2011, 2014; Kim et al., 2015). Therefore, we can investigate source dynamics once topography is considered in the modeling using an accurate digital elevation model (DEM). However, obtaining a high-resolution DEM at active volcanoes is challenging. DEMs derived using visible band sensors are generally the most cost-effective and feasible options for a remote island (Tanna, Vanuatu) and a highly active volcano (Yasur, explosions every 1–4 min), but the images we acquired for Yasur were obscured by both meteorological and volcanic clouds in the vent region. Additionally, the crater morphology can change over short periods of time due to the frequent explosions, thus requiring a DEM acquired near the time of the experiment. To account for this we combined DEMs created by (i) a UAV using structure-from-motion techniques within the crater (resolution 1.5 m); (ii) Worldview02 satellite stereo pairs collected on 26 September 2012 around the volcanic edifice (resolution 2 m); and (iii) ASTER Global (resolution 29 m) farther out from the crater and within the holes of the Worldview-derived DEM where clouds (both volcanic and meteorological) existed. These three DEMs were stitched together and smoothed in order to create a composite DEM. In the crater area where infrasound is most affected by topography, resolution was ~2 m. For computational reasons, the entire combined DEM was evenly resampled using 2-m grid spacing.

3.3. Inverse Model for the Acoustic Multipole Source Mechanism

The inversion method here follows that first proposed by Kim et al. (2015), which minimizes the misfit between the data and synthetic waveforms for a grid of trial source nodes over an assumed source region. We simulate the full 3-D numerical Green's functions (i.e., response from a simple source to receiver) for a monopole and horizontal and vertical dipole using FDTD modeling by solving a set of first-order, velocity-pressure coupled differential equations (Kim & Lees, 2011; Ostashev et al., 2005). The FDTD modeling follows Kim and Lees (2014) which incorporates the use of a DEM to account for realistic topography

and uses a graphics processing unit (GPU)-based approach in a compute unified device architecture (CUDA) environment, with compilation of the codes done using nvcc (NVIDIA compiler for CUDA-enabled codes). A simple source (Blackman Harris window function) with a cutoff frequency of 10 Hz is propagated over the aforementioned DEM (section 3.2). Earth's surface is treated as a rigid boundary, though in reality some energy is likely absorbed (Kim et al., 2012). The Perfectly Matched Layers technique is employed at the other model boundaries to create an absorbing boundary and remove reflections. The model grid is $2.2 \times 2.4 \times 0.5$ km with spacing of 2 m. This corresponds to 22 grid nodes per shortest wavelength in our filtered data (0.1–8 Hz), which is greater than the recommended minimum of 10 grid nodes (Wang, 1996). We use a grid search over 15×15 points with nodes spaced 15 m apart for the likely source location and pin these points to the DEM surface. Green's functions are computed for a duration of 6 s with a time step 0.001 s, which is long enough for the source to propagate well past all stations in the deployment. Sound speed and air density are assumed to be homogeneous at 346.4 m/s and 1.18 kg/m^3, respectively, based on a representative temperature value collected during the field campaign. Our method ignores wind and nonlinear behavior, which we examine further in section 5.

Acoustic pressure $p(\mathbf{x}_r, t)$ at distance $\mathbf{x}_r$ and time t can be represented by a monopole (mass flow rate) and the x, y, and z components of a dipole force given by Pierce (1989)

$$p(\mathbf{x}_r, t) = G(\mathbf{x}_r, t; \mathbf{x}_s) * \frac{\partial S(t)}{\partial t} + \frac{\partial G(\mathbf{x}, t; \mathbf{x}_s)}{\partial x_s} * F_x(t) + \frac{\partial G(\mathbf{x}, t; \mathbf{x}_s)}{\partial y_s} * F_y(t) + \frac{\partial G(\mathbf{x}, t; \mathbf{x}_s)}{\partial z_s} * F_z(t) \tag{2}$$

where $G(\mathbf{x}_r, t; \mathbf{x}_s)$ is the Green's function for a monopole, and $\mathbf{x}_r$ and $\mathbf{x}_s$ are the receiver and source position, respectively. Here, $S(t)$ is the mass flow rate at the source, and $F_x(t)$, $F_y(t)$, and $F_z(t)$ are the time histories of forces in x, y, and z directions, respectively. $\partial/\partial x_s$, $\partial/\partial y_s$, and $\partial/\partial z_s$ denote partial derivatives with respect to the source coordinate. The reader is referred to Morse and Ingard (1986) and Kim et al. (2012) for details on the monopole and dipole source mechanisms.

According to equation (2), the Green's functions for an arbitrary dipole, F_x, F_y, and F_z, can be defined by the spatial derivative of the monopole Green's function.

$$D_x \equiv \frac{\partial G(\mathbf{x}_r, t; \mathbf{x}_s)}{\partial x_s} \tag{3}$$

$$D_y \equiv \frac{\partial G(\mathbf{x}_r, t; \mathbf{x}_s)}{\partial y_s} \tag{4}$$

$$D_z \equiv \frac{\partial G(\mathbf{x}_r, t; \mathbf{x}_s)}{\partial z_s} \tag{5}$$

For the grid search method, the Green's functions G, D_x, D_y, and D_z can be determined by 3-D numerical simulation for every possible source location, which is computationally very expensive. Here, we use the reciprocal property of the Green's function (Morse & Ingard, 1986) to reduce the number of simulations. The reciprocity theorem leads to

$$G(\mathbf{x}, t; \mathbf{x}_s) = G(\mathbf{x}_s, t; \mathbf{x}) \tag{6}$$

$$\frac{\partial G(\mathbf{x}, t; \mathbf{x}_s)}{\partial x_s} = \frac{\partial G(\mathbf{x}_s, t; \mathbf{x})}{\partial x_s} \tag{7}$$

Therefore, instead of running 225 numerical simulations for the monopole Green's functions at the 15×15 source grid, we can obtain the same Green's functions by only seven simulations with a source at each receiver position. In addition, the dipole Green's functions can be calculated by spatial differentiation of the monopole Green's functions without additional simulations. The spatial derivatives of the Green's function can be further converted to temporal derivatives of particle motions by the first-order equation of motion (Morse & Ingard, 1986) that leads to

$$\frac{\partial p(\mathbf{x}, t)}{\partial x} = -\rho(\mathbf{x}) \frac{\partial v_x(\mathbf{x}, t)}{\partial t} \tag{8}$$

where $\rho(\mathbf{x})$ is the density, and $v_x(\mathbf{x}_s, t; \mathbf{x})$ is the x component of acoustic particle velocity. By substituting equation (8) in equation (6), the dipole Green's function can be rewritten as

$$D_x = \frac{\partial G(\mathbf{x}_s, t; \mathbf{x})}{\partial x_s} = -\rho(\mathbf{x}_s) \frac{\partial v_x(\mathbf{x}_s, t; \mathbf{x})}{\partial t} \tag{9}$$

and substituted back into equation (2) and similarly for the other two components (y and z). Because the output of numerical simulation is a time series, temporal differentiation is often more straightforward than spatial differentiation which requires additional time series at adjacent grid points. The model simulations output a pressure time history response to the Blackman Harris window function source recorded at the station, which we refer to as the 3-D Green's functions, similar to previous studies (e.g., Fee et al., 2017; Kim et al., 2015).

We perform a linearized waveform inversion using the observed acoustic data and Green's functions calculated in the previous steps to solve for the source location and multipole (monopole and dipole simultaneously) source time function using a grid search approach. Building on the methods of Kim et al. (2015) we use a simple rearranged version of equation (2)

$$\begin{bmatrix} G & D_x & D_y & D_z \end{bmatrix} \begin{bmatrix} \dot{S} \\ F_x \\ F_y \\ F_z \end{bmatrix} = \mathbf{Gm} = \mathbf{d} \tag{10}$$

where $\mathbf{m}$ is the solution vector of the mass flow rate and forces, $\mathbf{G}$ is the matrix representing the monopole and dipole Green's functions calculated from the FDTD forward model, and $\mathbf{d}$ is the observed acoustic pressures. Data are band-pass filtered between 0.1 and 8 Hz using a zero-phase filter and a window length of 5.5 s after the explosion onset. We zero each trace prior to the explosion onset and allow for slight discrepancies in arrival time at the stations (e.g., unaccounted for winds, temperature, station/vent location) by allowing a cross-correlation time-shift between Green's functions and observations of up to 0.04 seconds (a similar study by Fee et al. (2017) used 0.5 s).

The source location is determined by calculating the waveform misfit (residual) for the inversion using each grid point as the source location by solving the following equation using a LSQR iterative solver for linear equations (Paige & Saunders, 1982).

$$R = \frac{(\mathbf{d} - \mathbf{Gm})^T (\mathbf{d} - \mathbf{Gm})}{\mathbf{d}^T \mathbf{d}} \tag{11}$$

The grid point with the minimum residual is chosen as the preferred source location on the surface of the DEM. We perform the grid search inversion for the monopole-only source and use the grid point with the minimum residual as the source location for the multipole inversions. The inversion produces the expected synthetic acoustic waveform in pascals (Pa) at each station as well as the associated solution vector, or mass flow rate $S(t)$ in kilograms per second (kg/s), at the source. This mass flow rate is simply converted to a volume flow rate of displaced air (e.g., Fee et al., 2017; Johnson et al., 2008) using

$$V(t) = \frac{1}{\rho_{\text{air}}} \cdot S(t) \tag{12}$$

where $\rho_{\text{air}} = 1.18$ kg/m^3. Finally, we apply a simple linear trend correction to the final volume flow rate, detailed in the following section (section 3.4).

3.4. Signal Conditioning

For volcanic explosions, the recorded infrasound waveform's integrated compression (positive pressure) is not necessarily equivalent to that of the rarefaction (negative pressure). Therefore, while infrasound traces may taper to zero after an explosion has ceased, the integrated pressure (flow rate) may not go to zero after the explosion signal has ended. Consequently, the twice integrated pressure (cumulative flow rate) does not plateau, as it should under a linear assumption as mass is assumed to no longer be ejected from the vent. Johnson and Miller (2014) propose a signal correction technique, Finite Window Zero Pressure Zero Flux (FWZPZF), to mitigate the offset by performing a linear detrend on each station's waveform prior to performing the inversion. The detrend point for each station occurs where the integrated flow rate returns to
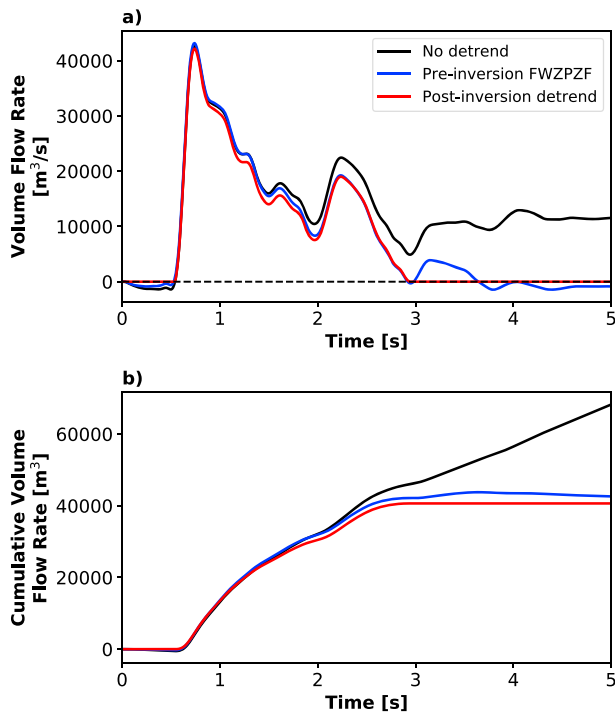
Figure 3. Comparison of linear detrending pre-inversion and post-inversion for an example Vent C explosion. (a) Shows the volume flow rate and (b) shows the cumulative volume, both as a function of time. The output of our inversion model without modification is shown in black, the inversion using the FWZPZF method of Johnson and Miller (2014) is shown in blue, and our proposed post-inversion linear correction is shown in red.

zero. This method is effective at removing the flow rate offset, but the detrend for each station is applied to waveforms prior to the inversion that contains both source and path effects. It is not viable for our multistation, grid search inversion incorporating numerical Green's functions and could lead to potential errors. Kim et al. (2015) removes the linear trend from the flow rate after the inversion but does not explore how this compares to the results following Johnson and Miller (2014) exactly. Fee et al. (2017) apply a linear detrend and demean to six stations using a different start and endpoint for each station following Johnson and Miller (2014). However, this simple detrend does not appear to bring the flow rate back to zero for all of the 49 explosions examined (see Figure 3 in Fee et al., 2017). Anderson et al. (2018) use a slightly different method for detrending where the optimal drift minimizes the L2 norm of the estimated flow rate:

$$q_t = H_{ij}(p_j - mt_j) \tag{13}$$

where q_t is the mass flow rate, H_{ij} is the ordinary least squares generalized inverse of the Green's functions, p_j is the recorded pressure, m is the slope of the instrument drift, and t_j is time.

Here we propose a linear detrend on the post-inversion flow rate that yields similar results to the FWZPZF method and does not rely on detrending the raw waveforms. We choose the first substantial increase in flow rate to be the start point for the linear detrend and the last value in the flow rate to be the end point of the detrend. We compare linear detrending both pre-acoustic and post-acoustic source inversion for an example explosion at Yasur in Figure 3. The linear trend correction both pre-inversion and post-inversion yields similar cumulative flow rates that level off after the explosion has ceased (as compared with the uncorrected inversion result). This figure also illustrates the necessity of detrending acoustic inversion results in general.

3.5. Event Selection

We select a limited number of explosions for inversion due to the high level of activity during the campaign and the computational cost of running the FDTD forward model for each of the aerostat sensor locations. Because the aerostat station location was different for each explosion, the Green's functions had to be uniquely calculated for each explosion. Out of the entire infrasound data set, we only searched for explosions during times when the aerostat station was tethered (and therefore the sensor location was well-constrained). To select events we apply a simple recursive STA/LTA (length of short-term average window = 0.005 s, length of long-term average window = 0.15 s) on the aerostat sensor data using a trigger threshold of 8, yielding a total of 201 events. Events are distinguished between the north and south crater based on the arrival times at the crater stations, which was later confirmed in the grid search inversion discussed in section 3.3. We then select 40 events for each vent and ensure a wide distribution of aerostat locations (Figure 2). We examine each event to confirm that the waveforms taper to zero and only one event is present during the 6-s time window. We see the same transition from predominantly Vent C (North crater) to Vent A (South crater) eruptions on 1 August mentioned in Jolly et al. (2017).

3.6. Evaluation of the Dipole Component

To help evaluate the significance of each dipole component (*x*, *y*, and *z*) to the source inversion, we calculate the Akaike Information Criterion (AIC). AIC evaluates the significance of free parameters in an inversion while imposing a penalty for increasing the number of model parameters to discourage overfitting the data. We follow the formula used in Ohminato et al. (1998)

$$AIC = N \cdot \log(S) + 2r \tag{14}$$

where N is the number of data points, S is the squared error for the whole waveform, and r represents the number of free parameters. AIC is a relative calculation in which the lowest AIC should be the ideal number
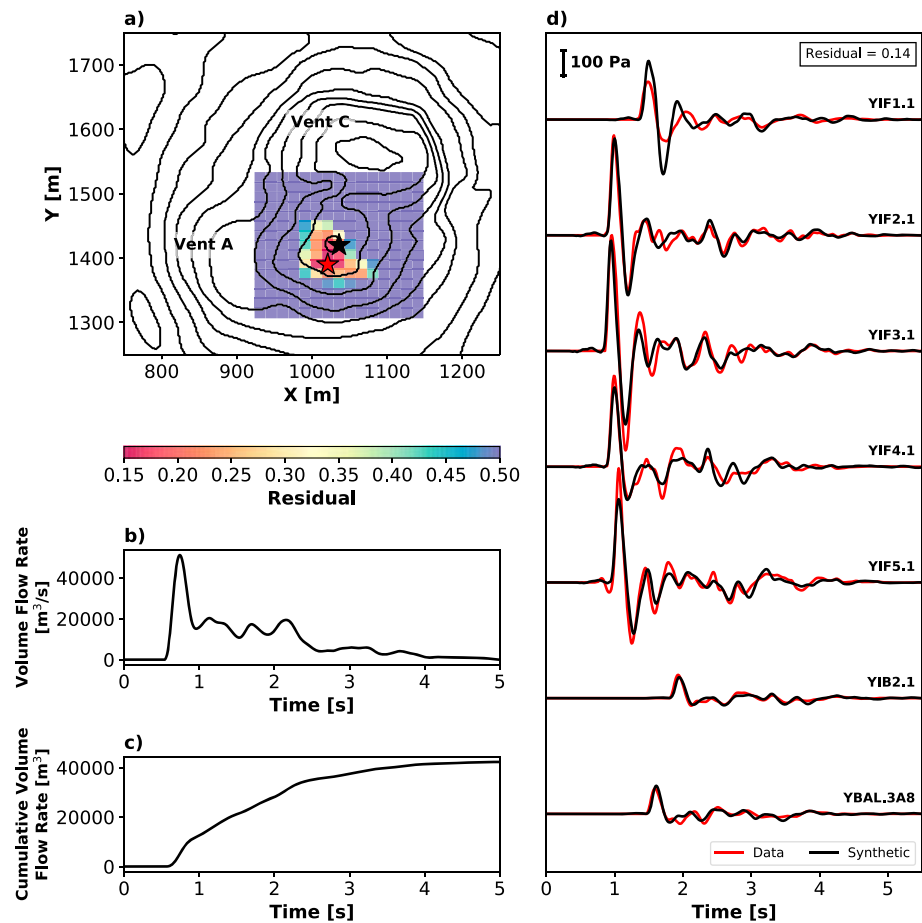
Figure 4. Monopole-only inversion results for event YBAL.3A8. (a) Residual map of the grid search for the best source location, yielding a minimum residual (red star) within 34 m of the low point of the DEM in the Vent A crater (black star). Grid cells are spaced 15 m apart in a 15 × 15 grid around the crater. Inferred (b) volume flow rate, and (c) cumulative erupted volume. (d) Data (red) and synthetic (black) waveforms for each station with an overall residual of 0.14 calculated using the full waveforms over the duration of 5.5 s.

of model parameters. We note that while adding the force components to a moment tensor inversion in seismology (i.e., going from six to nine free parameters) is an increase in number of parameters by 50%, our multipole acoustic inversion increases the number of free parameters from one (monopole only) to four (monopole and three dipole components), which is an increase in number of parameters in the inversion by 400%.

To further evaluate the dipole component and determine whether or not the inferred dipole vector has a dominant direction, we draw similarities with particle motion in seismology. We use rectilinearity (Montabetti & Kanasewich, 1970), defined as

$$F_r = 1 - \frac{\lambda_2}{\lambda_1} \tag{15}$$

where λ_1 is the principal eigenvalue (i.e., a measure of the long axis) and λ_2 is the second eigenvalue (i.e., a measure of the short axis). This equation yields results between 0 and 1, where $F_r = 1$ represents purely rectilinear motion. We set a threshold based on visual inspection of $F_r \geq 0.65$ to distinguish between events that have a dominant dipole direction from those that do not. The eigenvalues are calculated from the dipole time series from 0.5 to 1.5 s, which corresponds to the highest-amplitude oscillations of the dipole component for the explosions, and therefore the most likely time period of a dipole source mechanism, if it exists. The dominant direction is found by fitting a line in 3-D to the dipole solution using singular value decomposition (SVD), allowing for an azimuth and inclination to be determined using the first principal component. Explosions with directivity will likely have rectilinear acoustic dipole components.
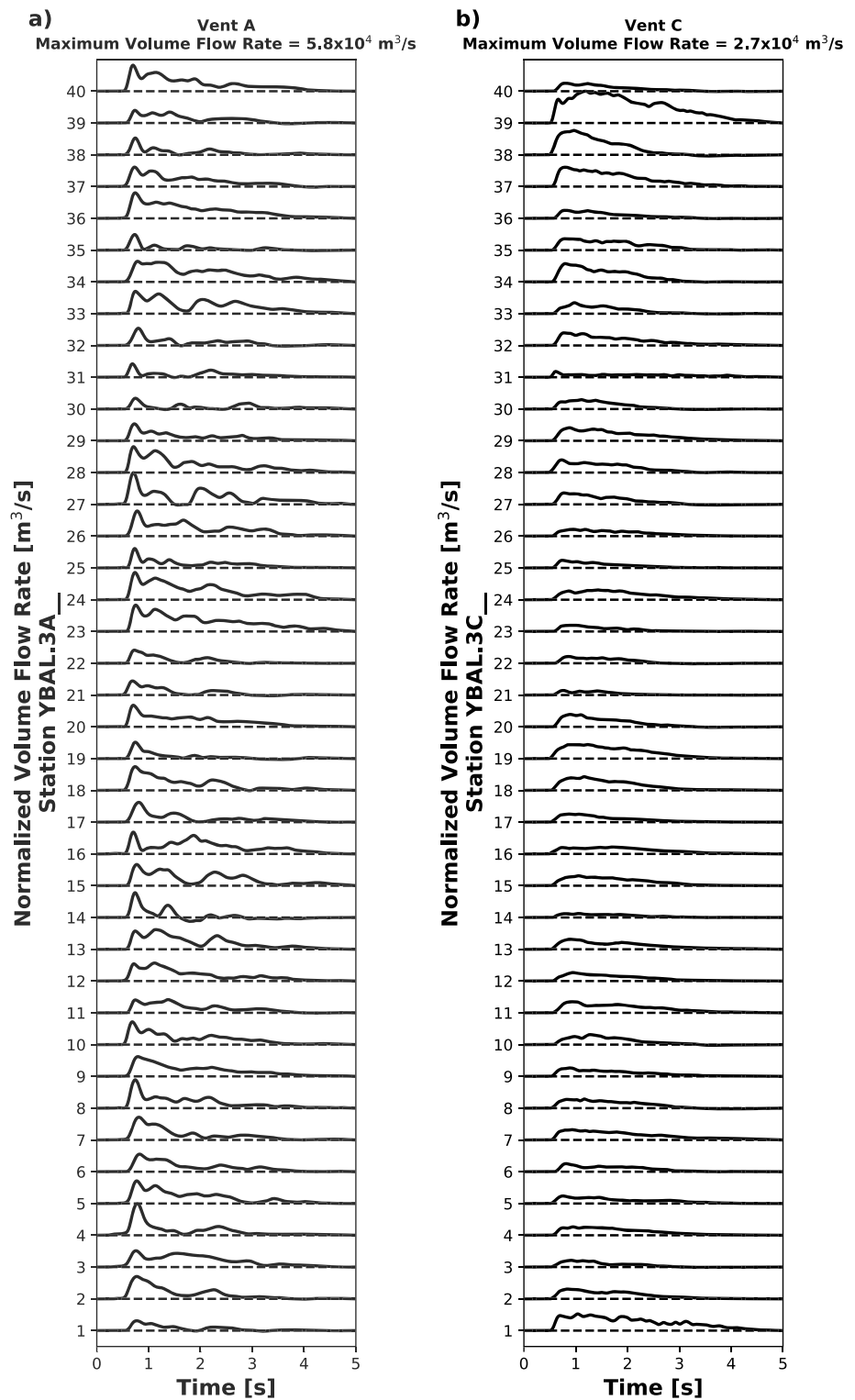
Figure 5. Volume flow rates ordered chronologically for selected events from (a) Vent A and (b) Vent C. Amplitudes are normalized to the peak of the largest event for each vent.

Table 1
Inversion Volume Flow Rate Summary for the 80 Events Used in This Study for Vents A and C

|		Vent A		Vent C	
		No topography	Topography	No topography	Topography
Monopole-only peak volume flow rate [10^4 m^3/s]	Range	1.9–6.1	1.8–5.8	0.37–3.6	0.33–2.7
	Average	4.1	3.7	1.1	0.91
Multipole peak volume flow rate [10^4 m^3/s]	Range	2.1–6.5	1.7–5.7	0.36–3.3	0.31–2.5
	Average	4.3	3.5	1.1	0.88
Monopole-only cumulative volume [10^4 m^3]	Range	1.2–7.8	1.3–7.5	0.30–5.9	0.38 – 5.7
	Average	4.0	4.0	1.3	1.4
Multipole cumulative volume [10^4 m^3]	Range	1.3–7.2	1.0–7.2	0.24–4.9	0.33–5.1
	Average	3.7	3.5	1.1	1.3
Monopole-only residual	Range	0.18–0.75	0.10–0.26	0.27–0.69	0.08–0.26
	Average	0.37	0.16	0.47	0.14
Multipole residual	Range	0.12–0.30	0.03–0.11	0.090–0.17	0.021–0.11
	Average	0.18	0.065	0.13	0.050

Additionally, we examine the stability of the inversions by varying the number of iterations the LSQR iterative solver completes before returning a solution **m**. We present these results as a convergence curve of the solution norm versus squared error (residual), in which the number of iterations that gives the solution closest to the corner of the convergence curve (i.e., location of maximum curvature) is the ideal number of iterations (e.g., Aster et al., 2013). We examine solutions for a select number of iterations to determine the dependence of the solution on the number of iterations performed, and therefore an estimate of stability of the inversion.

4. Results

4.1. Monopole Inversion

Waveforms for 80 explosions of Yasur volcano (40 per active vent) are inverted for the monopole acoustic source time function over a 15 × 15 grid of possible source locations. Results for example event YBAL.3A8 are shown in Figure 4. The 225 possible grid search source locations are colored by the squared error of the waveform fit, or residual, in Figure 4a where lower residuals correspond to a better fit to the data than source locations with higher residuals. The slight smearing of low residuals in the northwest-southeast directions is likely due to the lack of station coverage in those azimuths (station YIF6.1 that did not collect data during the aerostat campaign was located to the northwest), which decreased location constraint in that direction. The inversion source location (minimum residual, red star) is consistent with the assumed Vent A location at the DEM minimum in that subcrater (black star). The inferred source time function as the volume flow rate as a function of time is shown in Figure 4b, with a peak volume flow rate of 5.2×10^4 m^3/s and duration of ~2.5 s. The cumulative volume flow rate (i.e., integrated form of Figure 4b) is shown in Figure 4c, yielding a cumulative erupted volume of 4.4×10^4 m^3. In our model, the volume flow rate corresponds to the gas injection into the atmosphere. The waveform fit for the inversion is shown in Figure 4d, where the data are red and synthetics are black. The residual for this monopole-only inversion for the full waveform over 5.5 s is 0.14, which indicates a good fit to the data but other source terms might still be present that cannot be fit by an isotropic source. The relative arrival time of the initial compression between 1 and 2 s matches well for all stations; however, the amplitude of the initial compression of the synthetic waveforms differs from the data for some stations (e.g., YIF1.1, YIF4.1, and YIF5.1).

Inversion results for all 80 events show similarities and differences between the two active vents. Overall, the grid search method locates the events within ~30 m of the lowest point of the crater, or assumed vent location (Figure 4a, black star for Vent A). This confirms that events are from the correct active crater. We leave high resolution source location studies to other methods such as reverse time migration (e.g., Kim & Lees, 2014), as source location is not the main focus of this study. The normalized volume flow rates using the monopole inversion for explosions 1–40 for vents A and C are shown in Figures 5a and 5b, respectively. Vent A explosion volume flow rates generally have an abrupt onset that decreases rapidly during the first few tenths of a second, where Vent C explosion volume flow rates decrease more smoothly as a function of time.
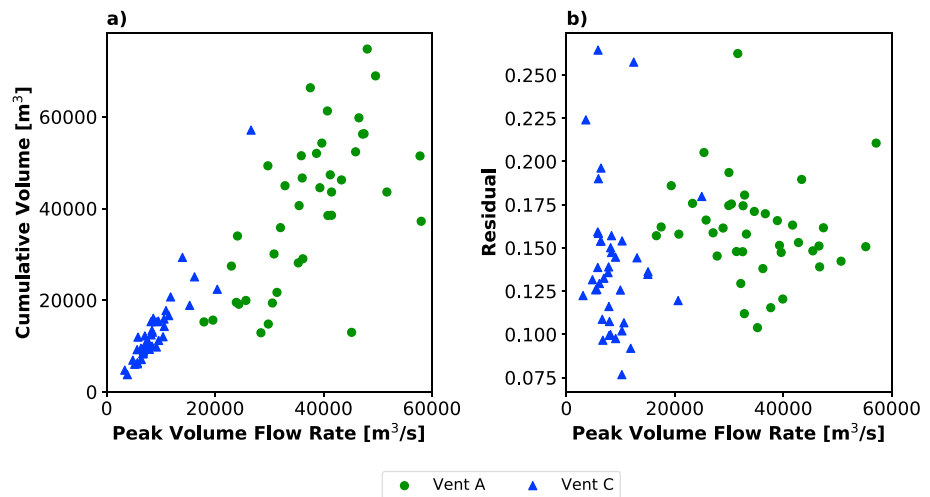
Figure 6. Comparison of monopole source inversion results for selected events. (a) Cumulative volume versus peak volume flow rate. (b) Residual versus peak volume flow rate. Vent A results are shown as green circles and Vent C results as blue triangles.

While explosion amplitudes cover a wide range for the 80 events investigated, volume flow rates have similar shape within each vent category, with a main onset that tapers back to zero after roughly 2.5–3 s. The average peak volume flow rate for 40 Vent A explosions is 3.7×10^4 m^3/s and average cumulative erupted volume is 4.0×10^4 m^3. Vent C explosion volume flow rates are smaller than Vent A, with an average peak volume flow rate of 9.1×10^3 m^3/s and average cumulative erupted volume is 1.4×10^4 m^3. The results are summarized in Table 1. Peak volume flow rate and cumulative volume for vents A and C are plotted in Figure 6a, indicating that events with higher peak volume flow rates tend to have higher cumulative volumes. Peak volume flow rates generally correlate with cumulative volumes. Peak volume flow rate does not appear to correlate with inversion residual in Figure 6b, suggesting that waveform fit is not dependent on the size of an eruption.

We next investigate the stability of the monopole inversions by changing the number of iterations performed in the LSQR iterative solver, ranging from 10 to 100,000 iterations. The monopole-only volume flow rate solutions are nearly identical and not dependent on the number of iterations used in the iterative solver, as shown in Figure S1 in the supporting information. Our stability test indicates that the solution converges fast and that small changes in fit to the data do not impact the volume flow rate solution.

4.2. Multipole Inversion

We perform a multipole (monopole and dipole in x, y, and z) acoustic waveform inversion for the same example event as the previous section (YBAL.3A8), finding that the multipole inversion provides a better fit to the data. The source location is set to the minimum-residual location determined by the monopole grid search to facilitate comparison with the monopole inversion (Figure 4). While not shown, a grid search for the multipole mechanism results in a less distinct minimum source location than the monopole inversion due to the increased number of model parameters. The multipole-derived volume flow rate as a function of time is shown in Figure 7a, with a peak volume flow rate of 5.1×10^4 m^3/s and duration of ~2.5 s, producing a cumulative volume of 4.0×10^4 m^3. The shape of the volume flow rate solution (solid line) is very similar to that of the monopole-only inversion solution (dotted line), with the peak and cumulative volume values being slightly smaller by 2.0% and 9.3%, respectively. This is a common trend for many events, as will be discussed below. The differentiated volume flow rate, which allows for the monopole and dipole sources to be more easily compared in the same physical dimension (acceleration), is shown by Figure 7b. The dipole forces in the x, y, and z directions are shown in Figures 7c–7e, yielding a peak dipole strength (sum of the squares of the forces in x, y, and z) of 6.4×10^7 N. The fact that the monopole and dipole source components are in phase suggests that the same physical source responsible for both, or that the inversion wants to partition the same source time function between monopole and dipole components. This can be interpreted as an explosion mechanism that is not perfectly omnidirectional (monopole) but has some directivity (dipole) structure to it. The vertical dipole that is larger than the horizontal dipoles may indicate a directional explosion in which the displaced fluid by jetting solid objects and gas/fluid phase is accelerated mainly in the
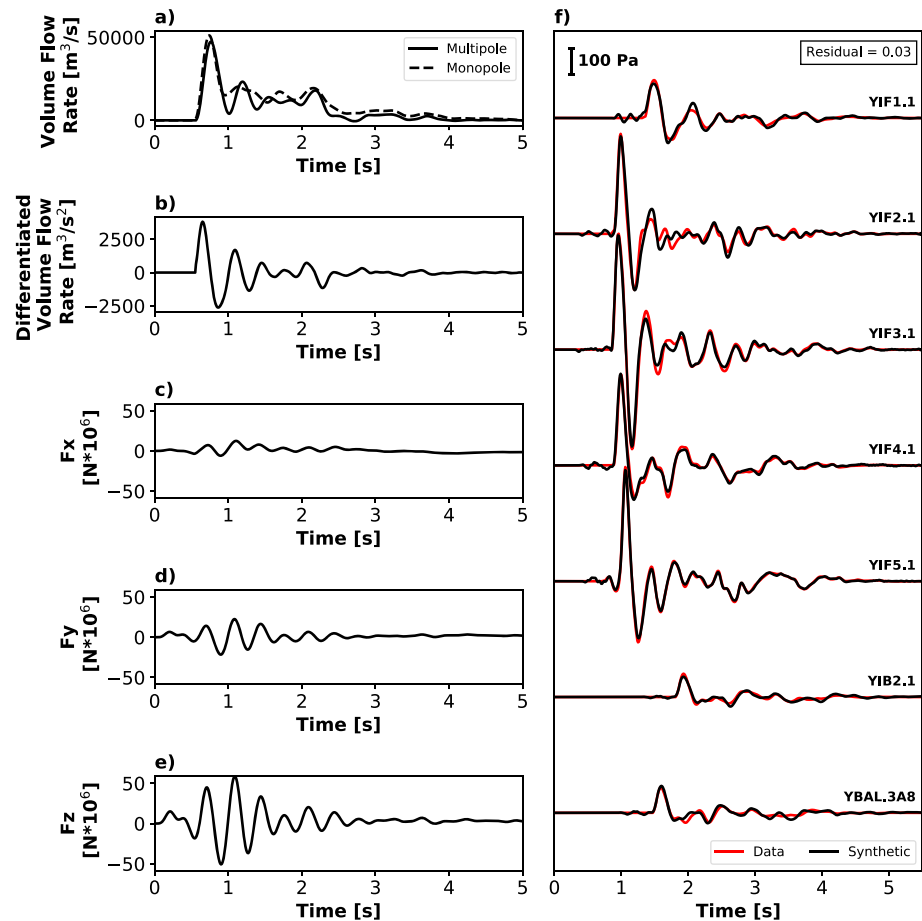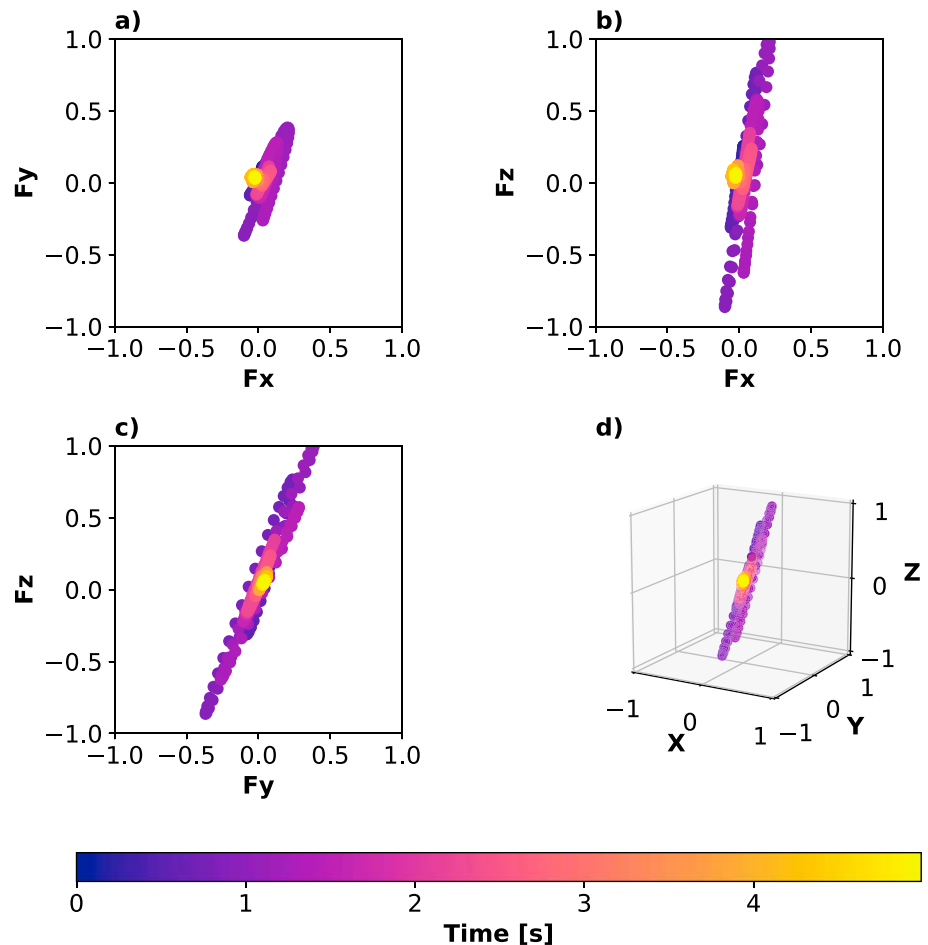
Figure 7. Inversion results for the multipole (monopole and three force components) for event YBAL.3A8. (a) Volume flow rate for the monopole component of the multipole inversion (solid line) and monopole-only inversion (dotted line). (b) Differentiated volume flow rate (acceleration). Force in (c) x, (d) y, and (e) z directions. (f) Data (red) and synthetic (black) waveforms for each station. A residual of 0.03 is calculated using the full waveforms over the duration of 5.5 s.

vertical direction (Chouet et al., 1974; Gerst et al., 2008; Johnson et al., 2008). The waveform fit for the multipole inversion for all stations is shown in Figure 7f. The residual has decreased to 0.03 for the multipole inversion from 0.14 for the monopole-only inversion and the amplitude of the synthetics for the first compression match the data well with the addition of the dipole components. These dipole components can be better visualized spatially in Figure 8. The inferred dipole for event YBAL.3A8 is predominantly positive in the vertical dimension and to the northeast, with an inclination of 67° from horizontal and azimuth of 19° clockwise from north. This event had a rectilinearity of 0.93, which is one of the highest rectilinearities and may indicate a strong dipole component for this explosion.

The volume flow rate solutions for the multipole inversions for all 80 events investigated in this study are similar in both magnitude and shape to that of the monopole-only inversion (Table 1). The peak volume flow rate and cumulative volume generally decrease slightly when the dipole components are added to the inversion. For Vent A, including the dipole components in the inversion causes an average decrease of 6.0% for peak volume flow rate and 11% in cumulative volume. For Vent C, the additional components, on average, decrease the peak volume flow rate by 2.7% and cumulative volume by 5.8%.

Vents A and C have distinct dipole characteristics both in amplitude and direction. Peak dipole strengths range between 6.8 and 75×10^6 N with an average of 3.3×10^7 N for Vent A and 2.4–25×10^6 N with an average of 6.1×10^6 N for Vent C. Explosions with higher peak volume flow rates tend to have higher peak dipole strengths (see Figure 9a, where peak dipole strength is plotted with peak volume flow rate). This is in agreement with the results of Figure 6b of Kim et al. (2012), where it is shown that events at Tungurahua

Figure 8. Dipole direction results for the multipole inversion (monopole and three force components) for event YBAL.3A8 in the three principal planes. (a) View of dipole in the *X-Y* plane. (b) View of dipole in the *X-Z* plane. (c) View of dipole in the *Y-Z* plane. (d) View of dipole in 3-D from a viewing azimuth of 300° and an elevation of 15°. Note, the coordinate system used is $+x$ (East), $+y$ (North), and $+z$ (up). Plots are normalized to the maximum dipole component value for the explosion and colored by time.

volcano with higher volume flux have higher dipole strengths. We note that Figure 9a also indicates that the dipole strength is substantially greater for Vent A than for Vent C events. A 3-D view of the dipole component of the multipole inversion for the first 12 events examined for each vent is shown in Figure 10. Explosions from Vent A not only have higher dipole strengths but also have a more defined dominant dipole direction than those from Vent C, meaning that the dipole more closely resembled a line in three dimensions (Figure 10). We further quantify the dipole direction using rectilinearity, where events that were considered to have a dominant dipole direction had rectilinearities greater than 0.65. Rectilinearities for Vent A ranged from 0.11–0.93, with an average of 0.71, while rectilinearities for Vent C ranged from 0.09–0.75 with an average of 0.47. Using a rectilinearity threshold of 0.65, 29 of 40 Vent A events and 6 of 40 Vent C events have dominant dipole directions. The rectilinearity is plotted as a function of peak dipole strength for Vents A and C (Figure 9b). Vent A explosions with high peak dipole strengths tend to have high rectilinearity as well. For low peak dipole strength for Vent A and most explosions from Vent C the trend is not very clear. This suggests that events with higher dipole strengths tend to have more defined dominant dipole directionality. It is unclear whether smaller events have less distinct directionality, or if it is just due to lower signal-to-noise ratio.

To further evaluate the significance of each dipole component (x, y, and z) to the source inversion, we calculate the AIC. AIC decreases as free parameters are added to the inversion (Table 2). This calculation suggests that all three dipole components lower the AIC score and may be the best solution according to the AIC calculation.
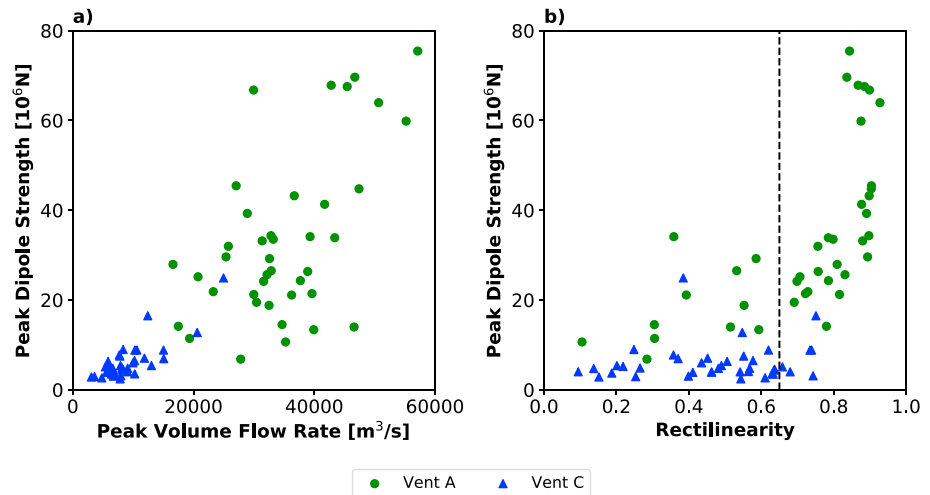
Figure 9. Comparison of monopole source inversion results for all events. (a) Peak dipole strength versus peak volume flow rate. (b) Peak dipole strength versus rectilinearity. Vertical dotted line in (b) denotes the $F_r \geq 0.65$ cutoff for events considered to have a dominant dipole direction.

AIC calculations for the majority of our multipole inversions show that the addition of dipole components in the source inversions lowers the AIC score. For Vent A, 26 of 40 events had AIC values for all four components less than that of the monopole-only inversion, while 17 of 40 events had the inversion with all four components as the minimum AIC overall (i.e., out of the monopole, monopole $+Fx$, monopole $+Fx+Fy$, and monopole $+Fx + Fy + Fz$). For Vent C, 39 of 40 events had AIC values for all four components less than the monopole only inversion, while 21 of 40 events had the inversion with all four components as the minimum AIC overall. These AIC calculations show that the addition of dipole components in the source inversion lowers the AIC score and likely not only fitting the noise. However, AIC is only one metric for evaluating inversions with increasing number of free parameters.

We also investigate the stability of the multipole inversion by varying the number of iterations in the LSQR iterative solver. A convergence curve of the norm of the solution ($||x||$) and squared error (residual) with respect to number of iterations for event YBAL.3A8 with the source location fixed is shown by Figure 11a. This curve illustrates that there are multiple local maximum curvature points as the number of iterations is increased (as opposed to the more traditional "L-shape"), creating a step-like pattern with jumps in solution norm corresponding to very small changes in residual. The volume flow rate, Fx, Fy, and Fz solution vectors are shown by Figures 11b–11e, respectively, for 100, 1,000, and 10,000 iterations. We find that the volume flow rate solution remains stable, even with an extreme case of 10,000 iterations (Figure 11b). This indicates that the volume flow values for monopole source are reliable, regardless of whether the dipole components are included in the source inversion or not. However, the dipole component solutions show large solution variations between iterations with small improvement in the data fitting (Figures 11c–11e).

4.3. Directionality

We explore the acoustic radiation pattern using simple waveform amplitude observations, specifically the difference in amplitude for the initial compression between the synthetic waveforms from the monopole inversion and the data (e.g., Figure 4d, stations YIF1.1, YIF4.1, and YIF5.1). Differences in amplitude between the data and model for the monopole inversion may be related to a dipole component or noise. We calculate this amplitude deviation (A_{dev}), or fractional misfit between the peak data compression amplitude ($A_d(t_{max,d})$) and corresponding synthetic value ($A_m(t_{max,d})$) divided by the peak data amplitude, for each station as follows

$$A_{dev} = \frac{A_d(t_{max,d}) - A_m(t_{max,d})}{A_d(t_{max,d})} \tag{16}$$

These percent differences are plotted as a function of azimuth from the vent for vents A (Figure 12a) and C (Figure 12b), where red corresponds to data amplitude being larger than the synthetics (i.e., synthetic underpredicts data amplitude) and blue denotes synthetic amplitude being larger than data amplitude (i.e.,
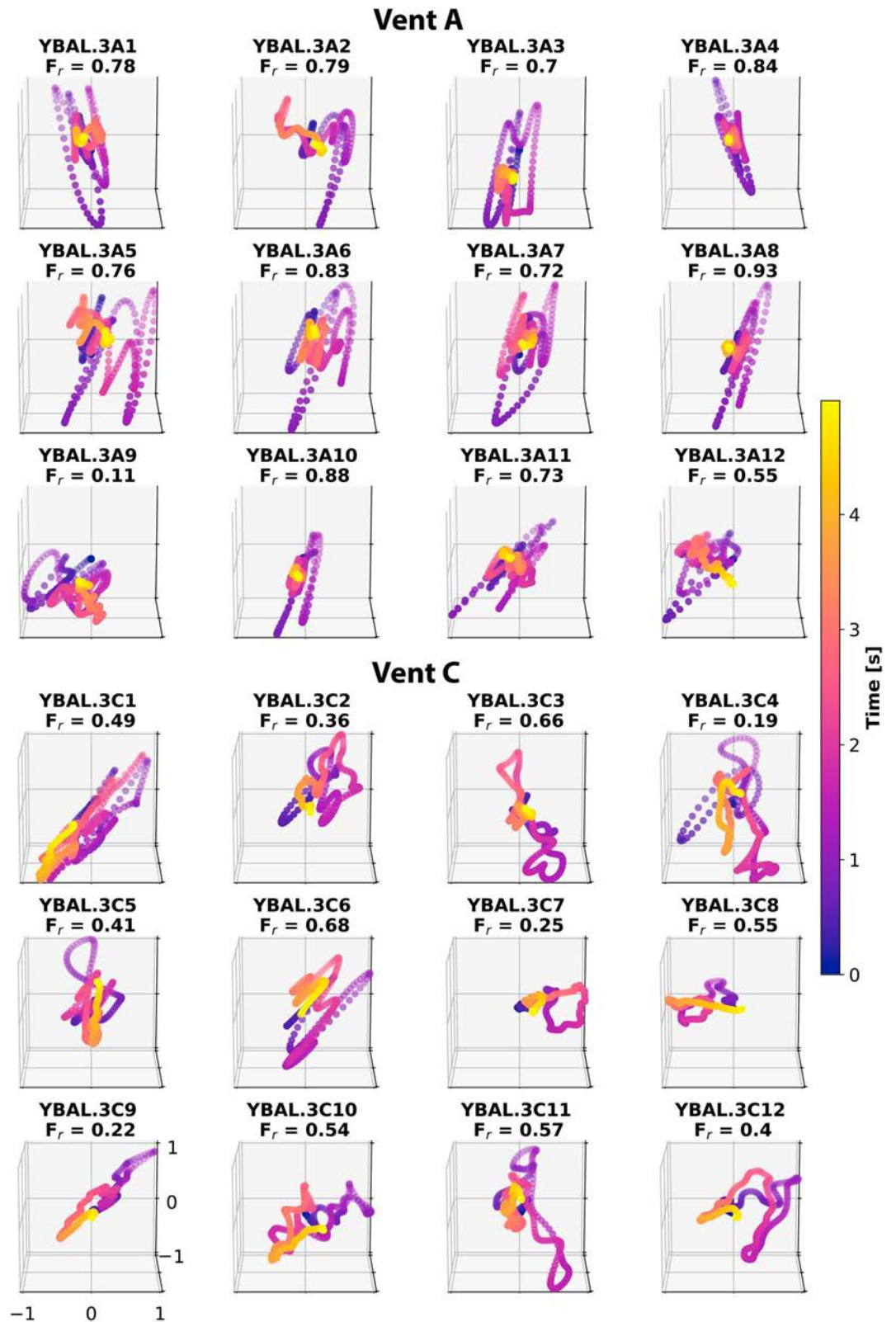
Figure 10. Visualization of the dipole component of the multipole inversion for the first 12 events investigated for both vents. The *x*, *y*, and *z* components of the dipole solution are normalized for each event to emphasize dipole solution shape, with axes labeled on the bottom left plot. Rectilinearity for each event is given by F_r.

Table 2
*AIC Calculation Using the Residual for the Entire Waveform for Example Event YBAL.3A8*

	Squared error	AIC
Monopole	0.14	−6520
Monopole + Fx	0.12	−6098
Monopole + Fx + Fy	0.07	−7067
Monopole + Fx + Fy + Fz	0.03	−9466

synthetic overpredicts data amplitude). This analysis shows that the monopole source mechanism underpredicts amplitudes to the east and south (e.g., YIF2-5) but overpredicts the amplitude to the north (e.g., YIF1.1), even after the effects of topography are accounted for in the synthetic waveforms.

4.4. Topographic Impact on Waveform Inversions

We rerun our source inversions using 1-D Green's functions obtained by simulating across a flat horizontal plane to assess the significance of topography on the Green's functions and inversion. This is the acoustic equivalent of a 1-D versus 3-D seismic ground motion simulation (e.g., Rodgers et al., 2018) to quantify path effects. The peak volume flow rate for example event YBAL.3A8 for a 1-D simulation is 5.7×10^4 m³/s, as compared to 5.2×10^4 m³/s for the 3-D simulation with topography. For this example, this results in a 8.7% decrease in peak volume flow rate when topography is included. We find that the peak volumetric flow rate for the 80 events examined in this study is overestimated by 10% for Vent A events and 16% for Vent C events. Additionally, waveform fit is worse when topography is not accommodated. The residuals for the 80 events explored in this study are, on average, 53% and 69% higher for vents A and C, respectively, for simulations propagated across a horizontal plane than when topography is considered. We summarize the values both with and without accounting for topography for peak volume flow rate, cumulative volume, and residual in Table 1.

A stability test and convergence curve is constructed for inversions propagated across a 1-D horizontal plane (Figure 13a). The inversion results for the volume flow rate remains stable and is not dependent on the number of iterations (Figure 13b). Figures 13c and 13d show similar solutions for the *Fx* and *Fy* components of the dipole that do not vary largely with number of iterations compared to the multipole inversion results across topography (Figures 11c and 11d). However, the vertical dipole (*Fz*) remains dependent on the number of iterations as shown in Figure 13e, making results unreliable with the given station coverage (only a single sensor on the tethered aerostat). These results indicate that the multipole inversion is more
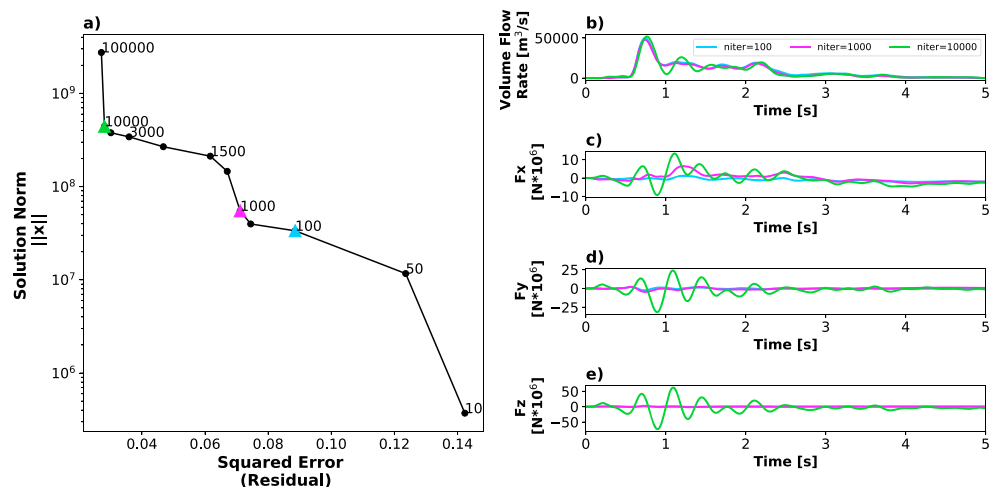
Figure 11. Multipole inversion stability test. (a) Convergence curve of the norm of the solution (‖*x*‖) and squared error (residual) with respect to number of iterations allowed by the least squares iterative solver for event YBAL.3A8. Panels (b)–(e) show the volume flow rate, *Fx*, *Fy*, and *Fz* solution vectors, respectively, for 100 (blue), 1,000 (pink), and 10,000 (green) iterations. Blue, pink, and green triangles in (a) correspond to volume flow rate vectors plotted in (b)–(e).
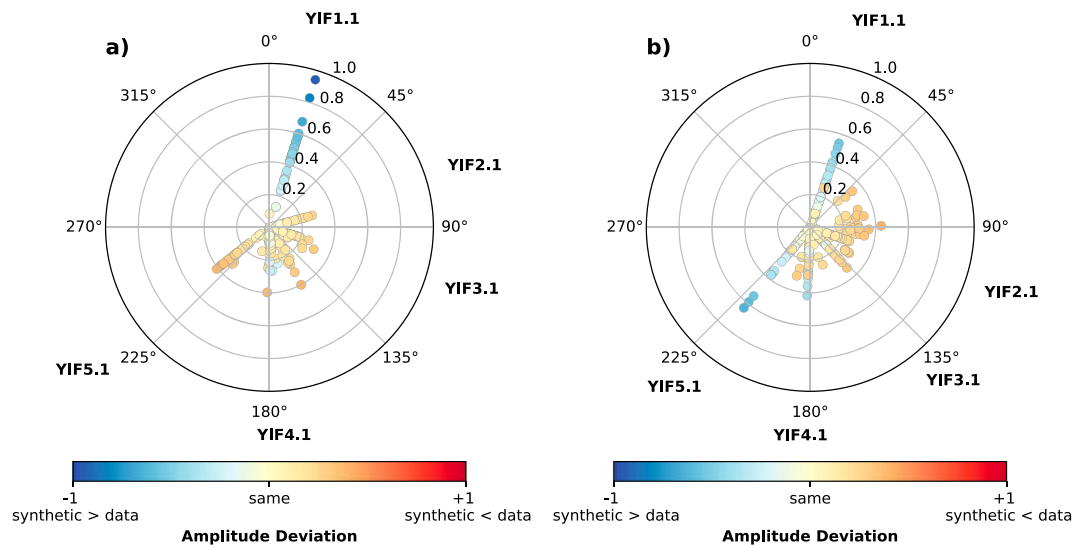
Figure 12. Difference in amplitude of the peak initial compression between modeled waveforms from a monopole-only inversion and the data for explosions from (a) Vent A and (b) Vent C. Positive differences signify that data amplitudes are higher than the model (red), while negative differences correspond to model amplitudes greater than the data (blue). Points near the center mean that the amplitudes match well, with zero being a perfect match.

stable with the Green's functions across a plane for the Fx and Fy components than when topography is accounted for, but the vertical dipole remains unstable. This increased stability may be due to those Green's functions being simpler than the Green's functions across topography, or possibly due to an effective dipole component induced by topography being better modeled by a single dipole approximation.

4.5. Contribution of the Aerostat Station to the Inversion

An enhanced characterization of the dipole component and acoustic directionality is afforded by including a sensor in the vertical dimension (in our case, aboard a tethered aerostat) that is not seen when only using stations placed on the Earth's surface (see Jolly et al., 2017, their Figure 1 for diagram of the tethered aerostat). Figure 14 shows the dipole component solution when the aerostat sensor is included for source inversion (top row, a–d) and when the aerostat sensor is not included (bottom row, e–h) for event YBAL.3A8. All components in Figure 14 are normalized to the global maximum across both inversions to facilitate visual comparison. Including the aerostat sensor yields a clear dominant dipole direction (Figures 14a–14d), while only
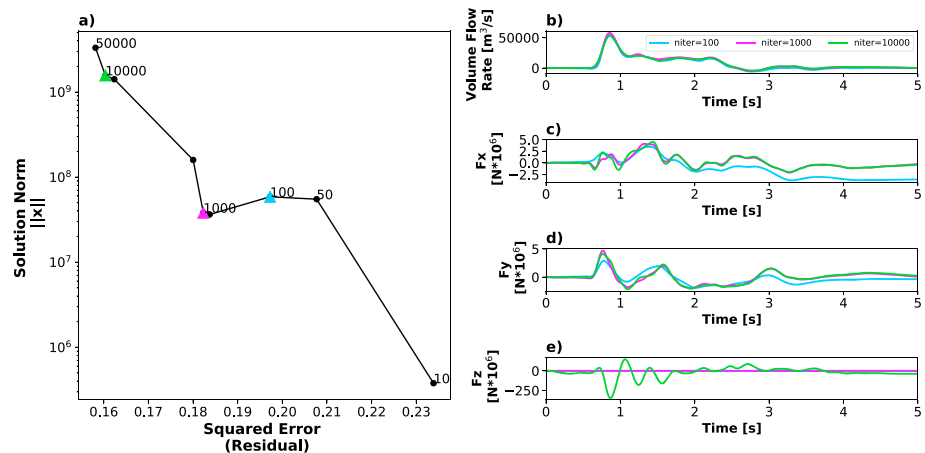
Figure 13. Multipole inversion stability test over a 1-D plane. (a) Convergence curve of the norm of the solution ($\|x\|$) and norm of the residual ($\|r\|$) with respect to number of iterations for event YBAL.3A8. Panels (b)–(e) show the volume flow rate, Fx, Fy, and Fz solution vectors, respectively, for 100 (blue), 1,000 (pink), and 10,000 (green) iterations. Blue, pink, and green triangles in (a) correspond to volume flow rate vectors plotted in (b)–(e). The Fz component is highly sensitive to the iteration number.
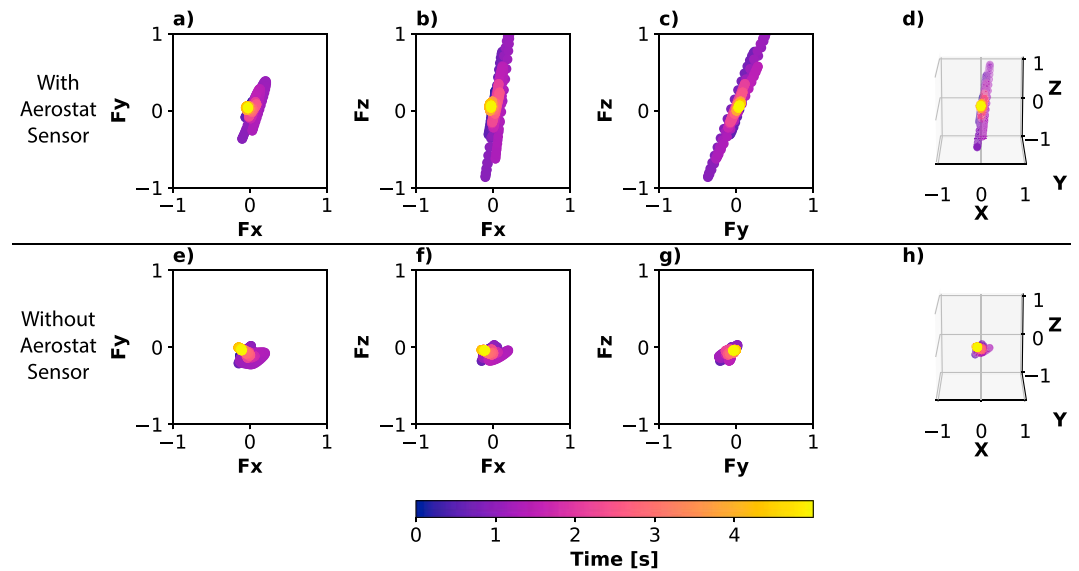
Figure 14. Comparison of dipole inversion results including the aerostat sensor in the inversion results (top row, a–d) and without (bottom row, e–h) for event YBAL.3A8. Components are normalized to the maximum of all components across both inversions. Dipole magnitude and directions are more pronounced when the aerostat sensor is included.

using the ground stations yields a much smaller dipole amplitude and less clear dominant dipole direction (Figure 14e–14h). Peak volume flow rate with and without the aerostat sensor is 5.1×10^4 m^3/s and 4.4×10^4 m^3/s, cumulative volume is 4.0×10^4 m^3 and 3.6×10^4 m^3, and peak dipole strength is 6.4×10^7 N and 1.8×10^7 N, respectively. These are all large differences, highlighting the potential importance of vertical sensors. We note that the aggregate residual decreases when the aerostat sensor is included in the multipole inversion, in this case from 0.14 to 0.03. Some individual events have a residual increase when the aerostat sensor is included in the inversion.

Similarly, we perform a "jackknife resampling" test for the entire network to assess bias in the inversion. We systematically remove each one of the seven sensors from the multipole inversion and compare results including peak volume flow rate, peak dipole strength, rectilinearity, and residual (Table 3). Rectilinearity and peak dipole strength remain high (>0.90 and >4.7×10^7 N, respectively) when YIB2.1, YIF3.1, or YIF2.1 are removed from the inversion. This indicates that the inversion is least sensitive to these stations, which happen to be in the middle of the azimuthal distribution of the stations deployed (Figure 2). Rectilinearity and peak dipole strength decrease greatly when YBAL.3, YIF5.1, or YIF1.1 are removed from the inversion, which are the three stations that stretch the azimuthal and vertical coverage of the deployment. We note that YIF1.1-YIF5.1 were located on the crater rim and therefore had similar vertical coverage, while YBAL.3

Table 3
Results of a Jackknife Resampling Test for the Multipole Inversion of Example Event YBAL.3A8

Excluded station	Peak volume flow rate (10^4 m^3/s)	Peak dipole strength (10^7 N)	Rectilinearity	Residual	Largest azimuthal gap (°)
None	**5.1**	**6.4**	**0.93**	**0.03**	**145**
YBAL.3	4.4	1.8	0.32	0.14	145
YIB2.1	5.1	6.3	0.93	0.16	145
YIF5.1	4.0	2.0	0.17	0.14	205
YIF4.1	4.4	1.7	0.51	0.14	145
YIF3.1	5.0	4.7	0.90	0.14	145
YIF2.1	5.0	6.7	0.95	0.16	145
YIF1.1	2.9	4.1	0.61	0.30	203

Note. Inversions were systematically performed using only six stations, each time with one station excluded from the inversion. The inversion result (boldface) for all seven stations is included as the first row for reference.

(aerostat) expands the vertical coverage of the network. A similar analysis for station configuration impact on source parameters is performed by Kim et al. (2012), where it was found that multipole inversions that do not account for topography are only stable if at least three stations spanning 180° around the infrasound source are used.

5. Discussion

The multipole acoustic source inversion can provide valuable information on a volcanic explosion source, yet the dipole components may be unstable even with good azimuthal ground station coverage and a station on a tethered aerostat. The acoustic monopole inversion is stable, converges fast, and solutions of volume flow rate are reliable given the network distribution of this Yasur volcano campaign (Figure S1). The monopole results are presented in the form of volume flow rate, which can easily be converted to mass flow rate (see Fee et al., 2017). Our grid search method indicates that the minimum-residual solution for most events is located within 30 m of the lowest point of the crater (i.e., our inferred vent location), demonstrating that events can easily be distinguished between the active vents at Yasur. Explosions from vents A and C show different characteristics from one another, but the shape and duration of explosion volume flow rates are similar to other explosions from the same vent. We find that Vent A explosions are larger and have volume flow rate peaks that decrease more rapidly than those from Vent C.

Although the dipole components may be unstable and/or nonexistent, we contend there is still utility in analyzing the dipole solutions and their importance to the overall acoustic source. By taking the optimal solution in the bend of the convergence curve, we make inferences on the source using the most reliable solution (albeit nonunique). The inclusion of the dipole components in the inversion yields results that indicate that a dipole component may exist for explosions at Yasur, even after topography is accounted for. We use rectilinearity as a measure of evaluating the dipole component, where events with higher rectilinearity were determined to have a dominant dipole direction. We find that 29 of 40 events from Vent A and only 6 of 40 events from Vent C had a dominant dipole direction according to this classification. Explosions from Vent A tend not only to have stronger directionality and a higher dipole strength, but also have a more linear motion as one would expect from a dipole source mechanism than explosions from Vent C. Furthermore, we show that inversions for the monopole solution (and hence volume flow rate) remain stable regardless of whether the inversion includes a monopole or a multipole (monopole and dipole) source mechanism. The shape and amplitudes of the volume flow rate for the monopole and multipole inversions are relatively similar (Figure 7a), despite dipole components being allowed to vary freely in the multipole inversion. The peak volume flow rate and cumulative volume generally decreased slightly when the dipole components were added to the inversion because part of acoustic pressure is attributed to the presence of a dipole, which does not generate the net change of mass in the source region.

Using an infrasound sensor elevated from the Earth's surface yields an unprecedented view of the acoustic wavefield from volcanic explosions, an idea proposed by Matoza et al. (2013). We use a tethered aerostat to achieve the vertical sensor coverage, but some studies such as McKee et al. (2017) and Rowell et al. (2014) have used nearby topography for an improvement in vertical station coverage for a network around a volcano. Including the aerostat sensor in the inversions yielded a measurable increase in dipole strength that would have otherwise been unobservable, and shows the importance of both the vertical sensor coverage and multipole inversion. For many explosions examined here, the peak dipole strength nearly doubled when the aerostat sensor was included in the source inversion. Inversions only using ground sensors often showed no realistic dipole component. There is a distinct dominant dipole when the aerostat sensor is used and a more random dipole shape when the aerostat sensor is excluded (see Figure 14). Therefore, 2-D source estimates of volcanic, and potentially anthropogenic, explosions may have underestimated (or at least poorly constrained) directionality. We caution that this study only uses one infrasound sensor hanging from a tethered aerostat as a proof-of-concept. Because of this, we performed a brief investigation to ensure that the calculated dominant dipole direction (azimuth and inclination) was not directly linked to the azimuth and inclination of the aerostat sensor as it moved to various loiter positions. While we do not see a strong correlation, future work should include more infrasound sensors in the vertical direction at varying azimuths and inclinations simultaneously to further sample the acoustic wavefield and constrain acoustic source directionality. For a dipole source, there are directions in which radiated acoustic energy density are greatest and some where radiated dipole energy cannot be detected (analogous to the nodal plane in a seismic moment tensor). Therefore, dense station coverage at a variety of azimuths and inclinations will be necessary for

future studies that perform acoustic waveform inversions with the intent to solve for a dipole solution, if it exists.

5.1. Reliability of the Dipole Component

Many acoustic source inversion studies have assumed that their inversions are stable due to good waveform fit, station coverage, etc. (e.g., Fee et al., 2017; Johnson et al., 2008; Johnson & Miller, 2014; Kim et al., 2015). However, our results and analysis suggest that the monopole solution is valid using numerical Green's function, but the dipole component(s) may still be unstable and nonunique. Including the dipole components causes decrease in residual by ∼0.10; however, the dipole components are highly dependent on number of iterations for our scenario (e.g., Figure 11) and station configuration (Table 3). This indicates that a small amount of noise in the data may change the dipole solution completely. Our results indicate that the multipole inversion as currently formulated may be ill-posed because the data we collected is not sufficient to fully constrain the source. Therefore, while our methods find a solution to the multipole inversion, we cannot uniquely determine that it is the true solution. Consequently, careful attention should be used for interpretations of our dipole results as they are nonunique. We caution that the commonly used (in volcano seismology) metric AIC which tests the significance of the number of free parameters can provide misleading results. Of the 80 events we explored, 65 have smaller "goodness of fit" AIC numbers for all four components than that of the monopole-only inversion. This reiterates that the model that provides the best fit (i.e., lowest residual) is not always the true solution (e.g., Aster et al., 2013; Bean et al., 2008; O'Brien et al., 2010). We stress that this is likely the case for many volcano deployments, as we use six ground stations with good azimuthal coverage as well as a sensor on a tethered aerostat, and still cannot reliably resolve the dipole component, if it exists. Stability analysis and sensitivity tests should be performed for future studies before the dipole component results can be considered reliable.

5.2. Eruption Directionality

In a volcanic environment, it is important to make a distinction between dipole radiation resulting from the source mechanism itself (e.g., the interaction of fluid with the vent walls and solid particles) (Caplan-Auerbach et al., 2010; Woulff & McGetchin, 1976) and that of an "effective dipole" where the environment directs acoustic radiation preferentially (e.g., diffraction and reflection of sound induced by topography, a subvertical conduit, or wind) (Kim et al., 2012). While we cannot reliably solve for the dipole components using an acoustic source inversion, we can make first-order observations about the unresolved amplitude differences from the monopole inversion that account for topography influences on the acoustic radiation pattern. Jolly et al. (2017) investigated explosions from Yasur during the same field experiment using both infrasound and video data to explore explosion directivity and found a high-amplitude infrasound anomaly at azimuths of ∼60–130° for explosions from the Vent C and ∼80–120° for explosions from Vent A (i.e., acoustic amplitudes are higher at the aerostat station than at the crater rim). They also find an increase in explosion amplitude for higher takeoff angles and that this amplitude anomaly exists for discrete explosions, as well as low-level (tremor-like) activity. However, they do not account for topography in their interpretations, so acoustic directivity seen in Jolly et al. (2017) could be due to path effects from topographic scattering by the crater walls (e.g., Kim et al., 2012) or from source directivity. The analysis of video data for ballistic trajectories that have consistent directionality to the east by Jolly et al. (2017) should remain true regardless of whether topography is considered for acoustic analysis. Our results are consistent with these findings, where the monopole source causes an underprediction of initial compression amplitudes toward the east and south but an overprediction the amplitude at YIF1.1 to the north for both vents (Figure 12). This shows that even though a reliable source inversion for the dipole or directionality cannot be performed, we see that explosions have directivity, and a monopole source cannot fully explain the data. Furthermore, this study indicates that multiple stations with excellent azimuthal coverage should be used, even for monopole source inversions, in order to obtain a more reliable estimate of the volume flow rate and other source parameters. Comparing our results directly to Jolly et al. (2017) is difficult as different events were used for the analysis of ballistic trajectories and those in this study. However, the existence of ballistic trajectory directionality supports our interpretation in our directionality results generally toward the east and south as ballistic trajectories may be less affected by topography than infrasound (like the amplitude ratio calculations of Jolly et al. (2017) can be) and are likely indicative of source directionality.

Our method aims to understand the acoustic radiation pattern of volcanic explosions and determine the relative influence of crater topography versus source mechanism on the observed directionality. While this method does not solve for the source physics causing that radiation, we briefly mention some potential

mechanisms. An explosion represented as a monopole is relatively easy to envision, whether it is a Strombolian gas bubble burst or any explosion that radiates infrasound equally in all directions. The physical representation of the volcanic dipole, however, is not as well understood. Johnson et al. (2008) attribute the dipole source of Strombolian explosions at Mt. Erebus to be the result of the random location of initial bubble membrane failure that leads to fluid advection. Jolly et al. (2016) explain infrasound source directivity from a mud heave as the result of a gas slug moving through a viscous mud/sulfur lake, though we note that station coverage was limited and topography effects were not accounted for in their study. If the vent opening is vertical, one would expect the vertical flow of material through the conduit to be modeled as a vertical dipole (Kim et al., 2012); however, a subvertically oriented conduit could cause a horizontal dipole component. Similarly, one might expect dipole radiation from a lateral blast, such as for the onset of the 1980 Mount St. Helens eruption (Lipman & Mullineaux, 1981). The ability to constrain a reliable dipole could yield information on ballistic directivity, as well as a more accurate calculation of volume flow rate via acoustic source inversion methods. While the dipole component at Yasur, if it exists, is likely small, larger eruptions could exhibit a larger dipole component, which may affect the calculation of volume flow rate to a greater extent.

5.3. Assumptions and Potential Sources of Error

Results highlighted in this study may have important implications for the volcano hazards community interested in calculating eruption mass via infrasound and source directivity, but there are still some notable assumptions and potential sources of error. In our inversion, we assume that once the effects of topography are incorporated into the calculation of 3-D Green's functions, the rest of the complexity in the waveform must be due to the source mechanism. In doing so, we assume a 1-D homogeneous atmosphere, that is, no winds or density changes. The farthest station we use in this study is roughly 1 km from the active vents, with most stations being within 0.5 km. At these short distances, winds would have to be very strong in order to have a measurable effect on the acoustic waveforms (Johnson & Ripepe, 2011; Kim et al., 2015; Kim & Lees, 2014). Jolly et al. (2017) note that winds were light (<10 m/s) and in the opposite direction (toward the west-northwest) of the observed directionality here.

We only account for linear sound propagation in our inversions. If nonlinear propagation was present (e.g., Marchetti et al., 2013), eruptive volumes would be underestimates of their true values (Anderson et al., 2018; Fee et al., 2017). Therefore, our results should be considered a minimum estimate where true volumes (and therefore masses) could be higher. Our inversion procedure yields low residuals even for high-amplitude events (>400 Pa at a distances less than 1 km from the vent). For each of the 80 events, we performed a grid search for the source location, yielding good agreement with the inferred vent location, meaning that waves likely did not surpass the speed of sound and propagate nonlinearly along most of the path (Fee et al., 2017). We assume that if a nonlinear component existed, it did not appear to last for a considerable amount of time and, therefore, nonlinear effects were likely weak (e.g., Fee et al., 2017).

Residuals for other recent monopole inversions such as Kim et al. (2015) and Fee et al. (2017) are smaller (generally <0.15, see Fee et al., 2017, Figure 4) than the ones calculated in this study (ranging from 0.08 to 0.26 for the monopole). We suggest this is because (i) Yasur may have a stronger dipole component; (ii) we have seven stations (compared to five and six of previous studies), including one on a tethered aerostat; and (iii) we are fitting higher frequencies than the other inversion studies (we filter between 0.1 and 8 Hz, while Kim et al. (2015) and Fee et al. (2017) use 0.001–2 Hz and 0.05–3 Hz, respectively). This also raises potential concern in assuming only a monopole source in the inversion as the true source mechanism may have higher order terms.

Due to the difficulty in obtaining a very accurate, high-resolution (<2 m) DEM in the visual band, we were forced to stitch together multiple DEMs from different methods (see section 3.2). Using other methods, such as LiDAR, which are not affected by residual steam and gas, would be preferable. We also note that topography can change between explosions over short time scales due to the frequent and explosive nature of Yasur, therefore the DEM should be created near the time of the field experiment. Another limitation of our inversion related to the DEM is that we assume a rigid topography. In reality near-surface layers have lower impedance.

Another potential source of error is the vertical location of the aerostat sensor. While the horizontal location (latitude and longitude) were recorded by the DATA-CUBE digitizer that was hanging from the tethered aerostat with the acoustic sensor, the vertical location was not recorded. Tests in similar atmospheric conditions were performed (outlined in Jolly et al., 2017) and indicate that vertical errors are on the order of

15 m while lateral errors are around 10 m. Given a reasonable speed of sound of 346 m/s, this yields arrival time errors on the order of 0.043 s vertically and 0.029 s horizontally. Our inversion uses a cross-correlation component which allows for timing errors up to 0.04s, as well as an individual grid search for each individual event to help mitigate the effect of aerostat and vent migration location errors on the inversion. We refer to Jolly et al. (2017) for a full description of how the vertical locations were calculated. Similarly, the main vents migrated as much as 20 m laterally over short time scales during this deployment (Jolly et al., 2017) as documented by daily UAV flyovers. These changes were also mitigated by this cross correlation component. Additionally, while our method accounts for potential vent migration between events by performing a grid search for the monopole-only inversion, we assume that the source is fixed during an explosion. Visual imagery suggests that the vents did not have measurable spatial variations within the explosions, however, there could be some spatial variation of the acoustic source over the course of a few seconds.

The events used in this study were discrete, short duration, Strombolian-type explosions. Due to the large number of explosions (thousands over the field campaign) and computational time for the FDTD calculation of the Green′s functions, we limited our study to 80 explosions with high signal-to-noise ratio and whose waveforms taper back to zero within a 6-s window. We also did not include time periods when measurable acoustic energy was emanating from both vents simultaneously. Future work should begin to expand acoustic source inversions to include more complex and sustained volcanic activity, including more energetic and hazardous eruptions. Additionally, this work would benefit greatly from a denser set of observations spatially and temporally. Our study also presents some of the first inversion results using infrasound sensors aboard a tethered aerostat, showing promise for their use in future experiments.

6. Conclusions

Two goals in volcano infrasound research we address in this study are (1) to invert acoustic data to infer erupted mass or mass eruption rate from an explosion and (2) to characterize the explosion directional radiation pattern. Here we assess the ability of typical network deployments and a new acoustic multipole inversion scheme that accounts for 3-D topography along with an acoustic sensor aboard a tethered aerostat to provide stable volcanic source constraints. We compare results for inversions that use a monopole-only source, multipole (monopole and dipole) source, propagation across a horizontal plane, and with varying station deployment geometries. We find that the monopole source mechanism is a good approximation for explosions at Yasur volcano as it is stable, reliable, and leads to relatively small waveform residuals when topography is included using numerical Green′s functions. The predominantly monopole explosions of Yasur Volcano are in agreement with previous studies of acoustic inversions that account for topography (e.g., Fee et al., 2017; Kim et al., 2015). We introduce a simple linear trend correction method applied post-inversion to detrend the volume flow rate solution. We find that Vents A and C have distinct characteristics, where both volume flow rate and dipole strength are substantially greater for Vent A than for Vent C events. Additionally, the peak dipole strength nearly doubled when the aerostat sensor was included in the source inversion, compared to a very small dipole component when only ground sensors where used. Therefore, 2-D deployments and subsequent source estimates of volcanic explosions may have underestimated and poorly constrained directionality. Our results indicate that inversions for the multipole source mechanism with all three dipole components (Fx, Fy, Fz) are unstable, even with an enhanced network that included an acoustic sensor on a tethered aerostat. We show that a nonunique multipole solution can be determined and metrics such as rectilinearity can be used to quantify them. We stress that improved waveform fits due to the inclusion of the dipole components as free parameters in subsequent calculations of AIC do not necessarily imply improved source inversion results. Stability of future acoustic inversions should be explored (e.g., Bean et al., 2008) before dipole components can be considered reliable and interpreted in their entirety. Even though a fully stable, unique source inversion for the dipole is not available here, we find that explosions exhibit directionality and that a monopole source, after topography is accounted for, cannot explain the data fully. First compression amplitude comparisons between data and synthetics show that amplitudes are underpredicted toward the east of the volcano and may therefore not be fully modeled by an isotropic source. This is consistent with ballistic directionality toward the east and likely represents explosion source directionality, which aids the understanding of eruption source dynamics and associated hazards. Furthermore, we reiterate that neglecting effects of topography especially in complex topographic regions such as volcanoes during acoustic waveform inversions leads to overestimation of the volume flow rate (e.g., Kim et al., 2015). These factors should be considered in future acoustic source studies, particularly

if used for volcano monitoring purposes to infer erupted mass of explosions. The effect of limited acoustic wavefield sampling should also be explored further using synthetic tests other real examples, both for volcanic and anthropogenic sources.

References

Albert, S., Fee, D., Firstov, P., Makhmudov, E., & Izbekov, P. (2015). Infrasound from the 2012–2013 Plosky Tolbachik, Kamchatka fissure eruption. *Journal of Volcanology and Geothermal Research*, *307*, 68–78. https://doi.org/10.1016/j.jvolgeores.2015.08.019

Anderson, J. F., Johnson, J. B., Ruiz, M. C., Ortiz, H. D., & Brand, B. D. (2018). Diverse eruptive activity revealed by acoustic and electromagnetic observations in the 14 July 2013 intense vulcanian eruption of Tungurahua (Ecuador). *Geophysical Research Letters*, *45*, 2976–2985. https://doi.org/10.1002/2017GL076419

Assink, J. D., Le Pichon, A., Blanc, E., Kallel, M., & Khemiri, L. (2014). Evaluation of wind and temperature profiles from ECMWF analysis on two hemispheres using volcanic infrasound. *Journal of Geophysical Research: Atmospheres*, *119*, 8659–8683. https://doi.org/10.1002/2014JD021632

Aster, R. C., Borchers, B., & Thurber, C. H. (2013). *Parameter estimation and inverse problems* (2nd ed.). New York: Elsevier.

Battaglia, J., Métaxian, J. P., & Garaebiti, E. (2016a). Families of similar events and modes of oscillation of the conduit at Yasur volcano (Vanuatu). *Journal of Volcanology and Geothermal Research*, *322*, 196–211. https://doi.org/10.1016/j.jvolgeores.2015.11.003

Battaglia, J., Métaxian, J. P., & Garaebiti, E. (2016b). Short term precursors of Strombolian explosions at Yasur volcano (Vanuatu). *Geophysical Research Letters*, *43*, 1960–1965. https://doi.org/10.1002/2016gl067823

Bean, C., Lokmer, I., & Brien, G. O. (2008). Influence of near-surface volcanic structure on long-period seismic signals and on moment tensor inversions: Simulated examples from Mount Etna. *Journal of Geophysical Research*, *113*, B08308. https://doi.org/10.1029/2007JB005468

Caplan-Auerbach, J., Bellesiles, A., & Fernandes, J. K. (2010). Estimates of eruption velocity and plume height from infrasonic recordings of the 2006 eruption of Augustine Volcano, Alaska. *Journal of Volcanology and Geothermal Research*, *189*(1-2), 12–18. https://doi.org/10.1016/j.jvolgeores.2009.10.002

Chouet, B., Dawson, P., & Arciniega-Ceballos, A. (2005). Source mechanism of Vulcanian degassing at Popocatépetl volcano, Mexico, determined from waveform inversions of very long period signals. *Journal of Geophysical Research*, *110*, B07301. https://doi.org/10.1029/2004JB003524

Chouet, B., Hamisevicz, N., & McGetchin, T. R. (1974). Photoballistics of volcanic jet activity at Stromboli, Italy. *Journal of Geophysical Research*, *79*(32), 4961–4976. https://doi.org/10.1029/JB079i032p04961

Dalton, M. P., Waite, G. P., Watson, I. M., & Nadeau, P. A. (2010). Multiparameter quantification of gas release during weak Strombolian eruptions at Pacaya Volcano, Guatemala. *Geophysical Research Letters*, *37*, L09303. https://doi.org/10.1029/2010GL042617

De Angelis, S., Lamb, O. D., Lamur, A., Hornby, A. J., von Aulock, F. W., Chigna, G., et al. (2016). Characterization of moderate ash-and-gas explosions at Santiaguito volcano, Guatemala, from infrasound waveform inversion and thermal infrared measurements. *Geophysical Research Letters*, *43*, 6220–6227. https://doi.org/10.1002/2016GL069098

Delle Donne, D., Ripepe, M., Lacanna, G., Tamburello, G., Bitetto, M., & Aiuppa, A. (2016). Gas mass derived by infrasound and UV cameras: Implications for mass flow rate. *Journal of Volcanology and Geothermal Research*, *325*, 169–178. https://doi.org/10.1016/j.jvolgeores.2016.06.015

Fee, D., Izbekov, P., Kim, K., Yokoo, A., Lopez, T., Prata, F., et al. (2017). Eruption mass estimation using infrasound waveform inversion and ash and gas measurements: Evaluation at Sakurajima Volcano, Japan. *Earth and Planetary Science Letters*, *480*, 42–52. https://doi.org/10.1016/j.epsl.2017.09.043

Fee, D., & Matoza, R. S. (2013). An overview of volcano infrasound: From Hawaiian to Plinian, local to global. *Journal of Volcanology and Geothermal Research*, *249*, 123–139. https://doi.org/10.1016/j.jvolgeores.2012.09.002

Gerst, A., Hort, M., Kyle, P. R., & Vöge, M. (2008). 4D velocity of Strombolian eruptions and man-made explosions derived from multiple Doppler radar instruments. *Journal of Volcanology and Geothermal Research*, *177*(3), 648–660. https://doi.org/10.1016/j.jvolgeores.2008.05.022

Johnson, J. B. (2003). Generation and propagation of infrasonic airwaves from volcanic explosions. *Journal of Volcanology and Geothermal Research*, *121*(1-2), 1–14. https://doi.org/10.1016/S0377-0273(02)00408-0

Johnson, J. B., Anderson, J., Marcillo, O., & Arrowsmith, S. (2012). Probing local wind and temperature structure using infrasound from Volcan Villarrica (Chile). *Journal of Geophysical Research*, *117*, D17107. https://doi.org/10.1029/2012JD017694

Johnson, J., Aster, R., Jones, K. R., Kyle, P., & McIntosh, B. (2008). Acoustic source characterization of impulsive Strombolian eruptions from the Mount Erebus lava lake. *Journal of Volcanology and Geothermal Research*, *177*(3), 673–686. https://doi.org/10.1016/j.jvolgeores.2008.06.028

Johnson, J. B., & Miller, A. J. C. (2014). Application of the monopole source to quantify explosive flux during Vulcanian Explosions at Sakurajima volcano (Japan). *Seismological Research Letters*, *85*(6), 1163–1176. https://doi.org/10.1785/0220140058

Johnson, J. B., & Ripepe, M. (2011). Volcano infrasound: A review. *Journal of Volcanology and Geothermal Research*, *206*(3-4), 61–69. https://doi.org/10.1016/j.jvolgeores.2011.06.006

Jolly, A., Kennedy, B., Edwards, M., Jousset, P., & Scheu, B. (2016). Infrasound tremor from bubble burst eruptions in the viscous shallow crater lake of White Island, New Zealand, and its implications for interpreting volcanic source processes. *Journal of Volcanology and Geothermal Research*, *327*, 585–603. https://doi.org/10.1016/j.jvolgeores.2016.08.010

Jolly, A. D., Matoza, R. S., Fee, D., Kennedy, B. M., Iezzi, A. M., Fitzgerald, R. H., et al. (2017). Capturing the acoustic radiation pattern of Strombolian eruptions using infrasound sensors aboard a tethered aerostat, Yasur volcano, Vanuatu. *Geophysical Research Letters*, *44*, 9672–9680. https://doi.org/10.1002/2017GL074971

Kim, K., Fee, D., Yokoo, A., & Lees, J. M. (2015). Acoustic source inversion to estimate volume flux from volcanic explosions. *Geophysical Research Letters*, *42*, 5243–5249. https://doi.org/10.1002/2015GL064466

Kim, K., & Lees, J. M. (2011). Finite-difference time-domain modeling of transient infrasonic wavefields excited by volcanic explosions. *Geophysical Research Letters*, *38*, L06804. https://doi.org/10.1029/2010GL046615

Kim, K., & Lees, J. M. (2014). Local volcano infrasound and source localization investigated by 3D simulation. *Seismological Research Letters*, *85*(6), 1177–1186. https://doi.org/10.1785/0220140029

Kim, K., Lees, J. M., & Ruiz, M. (2012). Acoustic multipole source model for volcanic explosions and inversion for source parameters. *Geophysical Journal International*, *191*, 1192–1204. https://doi.org/10.1111/j.1365-246X.2012.05696.x

Kim, K., & Rodgers, A. (2016). Waveform inversion of acoustic waves for explosion yield estimation. *Geophysical Research Letters*, *43*, 6883–6890. https://doi.org/10.1002/2016GL069624

Kremers, S., Lavallée, Y., Hanson, J., Hess, K. U., Chevrel, M. O., Wassermann, J., & Dingwell, D. B. (2012). Shallow magma-mingling-driven Strombolian eruptions at Mt. Yasur volcano, Vanuatu. *Geophysical Research Letters*, *39*, L21304. https://doi.org/10.1029/2012GL053312

Kremers, S., Wassermann, J., Meier, K., Pelties, C., van Driel, M., Vasseur, J., & Hort, M. (2013). Inverting the source mechanism of Strombolian explosions at Mt. Yasur, Vanuatu, using a multi-parameter dataset. *Journal of Volcanology and Geothermal Research*, *262*, 104–122. https://doi.org/10.1016/j.jvolgeores.2013.06.007

Lacanna, G., & Ripepe, M. (2013). Influence of near-source volcano topography on the acoustic wavefield and implication for source modeling. *Journal of Volcanology and Geothermal Research*, *250*, 9–18. https://doi.org/10.1016/j.jvolgeores.2012.10.005

Lamb, O. D., De Angelis, S., & Lavallée, Y. (2015). Using infrasound to constrain ash plume rise. *Journal of Applied Volcanology*, *4*(1), 1–9. https://doi.org/10.1186/s13617-015-0038-6

Le Pichon, A., Blanc, E., Drob, D., Lambotte, S., Dessa, J. X., Lardy, M., et al. (2005). Infrasound monitoring of volcanoes to probe high-altitude winds. *Journal of Geophysical Research*, *110*, D13106. https://doi.org/10.1029/2004JD005587

Lighthill, M. J. (1952). On sounds generated aerodynamically. I. General theory. *Proceedings of the Royal Society A, Mathematical, Physical and Engineering Science*, *211*(1107), 564–587. https://doi.org/10.1098/rspa.1952.0060

Lighthill, J. (1978). *Waves in fluids*. Cambridge: Cambridge University Press.

Lipman, P. W., & Mullineaux, D. R. (Eds.) (1981). *The 1980 Eruption of Mount St. Helens*. Washington: Geological Survey Professional Paper 1250.

Marchetti, E., Ripepe, M., Delle Donne, D., Genco, R., Finizola, A., & Garaebiti, E. (2013). Blast waves from violent explosive activity at Yasur volcano, Vanuatu. *Geophysical Research Letters*, *40*, 5838–5843. https://doi.org/10.1002/2013GL057900

Marcillo, O., Johnson, J. B., & Hart, D. (2012). Implementation, characterization, and evaluation of an inexpensive low-power low-noise infrasound sensor based on a micromachined differential pressure transducer and a mechanical filter. *Journal of Atmospheric and Oceanic Technology*, *29*(9), 1275–1284. https://doi.org/10.1175/JTECH-D-11-00101.1

Matoza, R. S., Fee, D., Garcés, M. A., Seiner, J. M., Ramón, P. A., & Hedlin, M. A. H. (2009). Infrasonic jet noise from volcanic eruptions. *Geophysical Research Letters*, *36*, L08303. https://doi.org/10.1029/2008GL036486

Matoza, R., Fee, D., Green, D., & Mialle, P. (2019). Volcano Infrasound and the International Monitoring System. In A. Le Pichon, E. Blanc, & A. Hauchecorne (Eds.), *Infrasound monitoring for atmospheric studies* (pp. 1023–1077). Cham.: Springer.

Matoza, R. S., Fee, D., & Lopez, T. M. (2014). Acoustic characterization of explosion complexity at Sakurajima, Karymsky, and Tungurahua volcanoes. *Seismological Research Letters*, *85*(6), 1187–1199. https://doi.org/10.1785/0220140110

Matoza, R. S., Fee, D., Neilsen, T. B., Gee, K. L., & Ogden, D. E. (2013). Aeroacoustics of volcanic jets: Acoustic power estimation and jet velocity dependence. *Journal of Geophysical Research: Solid Earth*, *118*, 6269–6284. https://doi.org/10.1002/2013JB010303

Matoza, R. S., Garces, M. A., Chouet, B. A., D'Auria, L., Hedlin, M. A. H., De Groot-Hedlin, C., & Waite, G. P. (2009). The source of infrasound associated with long-period events at mount St. Helens. *Journal of Geophysical Research*, *114*, B04305. https://doi.org/10.1029/2008JB006128

McKee, K., Fee, D., Yokoo, A., Matoza, R. S., & Kim, K. (2017). Analysis of gas jetting and fumarole acoustics at Aso volcano, Japan. *Journal of Volcanology and Geothermal Research*, *340*, 16–29. https://doi.org/10.1016/j.jvolgeores.2017.03.029

Meier, K., Hort, M., Wassermann, J., & Garaebiti, E. (2016). Strombolian surface activity regimes at Yasur volcano, Vanuatu, as observed by Doppler radar, infrared camera and infrasound. *Journal of Volcanology and Geothermal Research*, *322*, 184–195. https://doi.org/10.1016/j.jvolgeores.2015.07.038

Métrich, N., Allard, P., Aiuppa, A., Bani, P., Bertagnini, A., Shinohara, H., et al. (2011). Magma and volatile supply to post-collapse volcanism and block resurgence in Siwi caldera (Tanna Island, Vanuatu arc). *Journal of Petrology*, *52*(6), 1077–1105. https://doi.org/10.1093/petrology/egr019

Montabetti, J. F., & Kanasewich, E. R. (1970). Enhancement of teleseismic body wave phases with a polarisation analysis. *Geophysical Journal Royal Astronomical Society*, *21*(July), 119–129. https://doi.org/10.1111/j.1365-246X.1970.tb01771.x

Morse, P. M., & Ingard, K. U. (1986). *Theoretical acoustics*. Princeton, NJ: Princeton University Press.

O'Brien, G. S., Lokmer, I., & Bean, C. J. (2010). Statistical selection of the "best" seismic source mechanisms from inversions of synthetic volcanic long-period events. *Journal of Geophysical Research*, *115*, B09303. https://doi.org/10.1029/2009JB006958

Ohminato, T., Chouet, B. A., Dawson, P. B., & Kedar, S. (1998). Waveform inversion of very-long-period impulsive signals associated with magmatic injections beneath Kilauea volcano, Hawaii. *Journal of Geophysical Research*, *103*(10), 23,839–23,862. https://doi.org/10.1029/98JB01122

Ortiz, H. D., Johnson, J. B., Ramón, P. G., & Ruiz, M. C. (2018). Using infrasound waves to monitor tropospheric weather and crater morphology changes at Volcán Tungurahua, Ecuador. *Journal of Volcanology and Geothermal Research*, *349*, 205–216. https://doi.org/10.1016/j.jvolgeores.2017.11.001

Ostashev, V. E., Wilson, D. K., Liu, L., Aldridge, D. F., Symons, N. P., & Marlin, D. (2005). Equations for finite-difference, time- M. A. numerical implementation. *The Journal of the Acoustical Society of America*, *117*, 503–517. https://doi.org/10.1121/1.1841531

Paige, C. C., & Saunders, M. A. (1982). LSQR: An algorithm for sparse linear equations and sparse least squares, *ACM Trans. Math. Softw.*,*8*(1), 43–71, https://doi.org/10.1145/355984.355989

Pierce, A. D. (1989). *Acoustics: An introduction to its physical properties and applications*. Melville, NY: Acoustical Society of America.

Rodgers, A. J., Pitarka, A., Petersson, N. A., Sjögreen, B., & McCallen, D. B. (2018). Broadband (0–4 Hz) ground motions for a magnitude 7.0 Hayward fault earthquake with three-dimensional structure and topography. *Geophysical Research Letters*, *45*, 739–747. https://doi.org/10.1002/2017GL076505

Rowell, C. R., Fee, D., Szuberla, C. A. L., Arnoult, K., Matoza, R. S., Firstov, P. P., et al. (2014). Three-dimensional volcano-acoustic source localization at Karymsky Volcano, Kamchatka, Russia. *Journal of Volcanology and Geothermal Research*, *283*, 101–115. https://doi.org/10.1016/j.jvolgeores.2014.06.015

Simkin, T., Siebert, L., McClelland, L., Bridge, D., Newhall, C., & Latter, J. H. (1981). *Volcanoes of the world: A regional directory, gazetteer, and chronology of volcanism during the last 10,000 years*. Pennsylvania: US Hutchinson Ross Publishing.

Wang, S. (1996). Finite-difference time-domain approach to underwater acoustic scattering problems. *Journal of the Acoustical Society of America*, *99*(4), 1924–1931. https://doi.org/10.1121/1.415375

Witsil, A. J. C., & Johnson, J. B. (2018). Infrasound explosion and coda signal investigated with joint analysis of video at Mount Erebus, Antarctica. *Journal of Volcanology and Geothermal Research*, *357*, 306–320. https://doi.org/10.1016/j.jvolgeores.2018.05.002

Woulff, G., & McGetchin, T. R. (1976). Acoustic noise from volcanos—Theory and experiment. *Geophysical Journal of the Royal Astronomical Society*, *45*(3), 601–616. https://doi.org/10.1111/j.1365-246X.1976.tb06913.x